Journal of Computational Physics (2018)

Contents lists available at ScienceDirect

Journal of Computational Physics

journal homepage: www.elsevier.com/locate/jcp

Modal explicit filtering for large eddy simulation in discontinuous spectral element method

Zia Ghiasi[a], Jonathan Komperda[a], Dongru Li[a], Ahmad Peyvan[a], David Nicholls[b], Farzad Mashayek[a,*]

[a]Department of Mechanical and Industrial Engineering, University of Illinois at Chicago, Chicago, IL 60607, United States
[b]Department of Mathematics, Statistics and Computer Science, University of Illinois at Chicago, Chicago, IL 60607, United States

ARTICLE INFO

Article history:

Keywords:
Spectral element method
Turbulence
Large eddy simulation
Explicit filter
Modal filter

ABSTRACT

Developing a turbulence model that is computationally inexpensive and compatible with the nature of the numerical scheme is a crucial step in expanding the application of spectral element methods for large eddy simulation (LES) in complex geometries. In this paper, an element-level modal low-pass explicit filtering procedure, which operates in the spectral space, is implemented in a discontinuous spectral element method (DSEM). The application of the modal filter is studied for LES without a subgrid-scale (SGS) model. The method is tested for a configuration featuring isotropic turbulence, and its performance is compared with a previously used method—a spectral interpolation-based nodal filter. The modal filter shows superior performance over the nodal filter. The filtering procedure is also applied to a turbulent channel flow at a friction Reynolds number of $Re_\tau = 544$, and the results are compared with a previous direct numerical simulation (DNS). It is also shown that the filter strength that provides the best comparison with DNS depends only on the polynomial order and is not a function of the grid resolution. An anisotropic version of the modal filter, which damps high-frequency modes in a specific direction, is also introduced and tested for the channel flow. It is observed that filtering in the spanwise direction is the most effective approach based on the comparison of velocity mean and fluctuations with DNS. In general, the modal filter has shown good performance for both isotropic and wall-bounded flows; the calculated channel friction Reynolds number for the modal filter is within 0.26% error with respect to the DNS data, compared to 5.8% error for a case with no modeling.

*Corresponding author: Tel.: +1-312-996-1154;
e-mail: mashayek@uic.edu (Farzad Mashayek)

1. Introduction

In large eddy simulation (LES) of turbulent flows, the motions with larger scales are directly calculated, while the effects of the small-scale motions are modeled [1]. The governing equations of the large-scale motions of the flow are obtained by applying a spatial low-pass filter to the Navier-Stokes equations [1]. The filter divides the flow scales into two parts: resolved and subfilter-scale (SFS) motions [2]. These regions are shown in Fig. 1. The most widely used approach for LES is to consider the coarse computational mesh as the spatial low-pass filter. This type of filter is called an implicit filter since no explicit filtering operation is applied in the procedure [1]. For the case of the implicit filter, SFS would be equivalent to the scales smaller than the grid size, the so-called subgrid-scales (SGS); see Fig. 1. Even though the implicit filtering approach takes full advantage of the grid resolution, the shape of the low-pass filter is not known [2]. Another drawback of the implicit filtering approach is that there is no direct control on the energy spectra in the high-wavenumber motions [1]. To address the issues attributed to implicit filtering, explicit filtering is often introduced; a low-pass filter, with a filter width larger than the grid size, is explicitly applied to the flow variables. The explicit filtering approach provides a well-defined filter shape at the cost of reducing the effective resolution of the simulation compared with the grid resolution [1, 3]. Since the filter width is larger than the grid size, the SFS motions are divided into resolved subfilter-scale and unresolved subfilter-scale motions. The latter is equivalent to the SGS motions. The use of an explicit filter is practiced in LES studies and is shown to reduce the numerical error [3, 4] as well as aliasing and SGS modeling errors [3] and improve the accuracy of LES results [2, 3, 5]. Gullbrand and Chow [2] performed LES of turbulent channel flow using a finite difference (FD) code. They showed that using explicit filtering potentially limits the effects of the numerical errors in dynamic Smagorinsky [6] and dynamic reconstruction models and significantly improves the accuracy of the mean velocity and turbulence intensities. In both cases of LES with implicit and explicit filtering, the effects of the motions of the unresolved scales should be taken into account. Those effects, which appear as the SGS stress tensor in the governing equations, are commonly modeled by a SGS model, such as an eddy-viscosity model [7, 8, 6] or a similarity model [9].

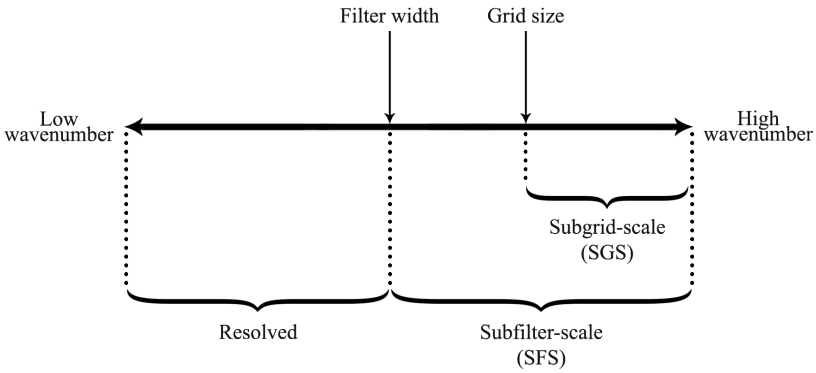

Fig. 1: The division of turbulence motions by the filter and the grid based on their wavenumbers.

An alternative approach that is gaining more attention recently is a form of LES known as implicit LES (ILES). In this approach, the dissipation of the numerical scheme is assumed to mimic the effects of the viscous dissipation of the SGS motions and dampen the turbulent energy. Even though, ILES has shown successful results [10, 11, 12, 13], the damping effects on the resolved scales remain questionable. This method is also not suitable for high-order schemes that introduce minimal or no numerical dissipation. Winters *et al.* [14] studied the ILES capabilities of discontinuous Gelerkin (DG) methods for under-resolved DNS (uDNS) of very high Reynolds number turbulence. In the absence of sufficient dissipation, the accumulation of the energy at the grid cutoff wavenumber results in numerical errors and could lead to instabilities [1]. To alleviate this problem, an explicit low-pass filter can be applied to the solution variables to remove the small-scale components of the solution. In this approach, which is used in the present work, the explicit filtering serves as a drain for the energy cascade and prevents the instabilities. This approach reduces the computational cost as well as implementation complexity compared to methods that use a SGS model. Using an explicit filter without any SGS model has been practiced for LES studies. Bogey and Baily [15] conducted high-order finite difference simulation of compressible jets using an explicit filter without any SGS model. They applied the filter to the density, velocities, and pressure every two time steps, sequentially in x-, $y-$, and z-directions. Mathew

et al. [16] applied an explicit filter on the solution variables at every time step for LES of compressible channel flows. However, they mention that a finite number of time steps can be taken without applying the filter. Fischer and Mullen [17] applied an explicit interpolation-based nodal filter to stabilize their spectral element method and used it for LES of complex flows [18]. Later, Sengupta [19] used the same filtering approach without a SGS model for LES of isotropic turbulence and compared the results with the dynamic Smagorinsky model [8]. Sengupta *et al.* [20] used the same procedure for the LES of flow over a backward-facing step.

The benefit of explicit filtering is realized especially in high-order methods such as discontinuous spectral element methods (DSEM). The negligible numerical dissipation in these methods demands a drain for the energy cascade to avoid numerical instabilities in under-resolved simulations. The basis functions in spectral methods form a hierarchical set, i.e., they represent progressively higher spatial frequencies. Therefore, a sharp cutoff of the higher modes in the modal space (a modal filter) represents a low-pass spatial filter of the solution in the nodal space. Boyd [21, 22] applied a modal filter in his spectral method to reduce Gibbs oscillations that are produced by shocks. Levin *et al.* [23] applied a two-step modal filter to inhibit the growth of instabilities in their eddy resolving spectral element ocean model. Blackburn and Schmidt [24] used a modal filter in their spectral element method as the test filter of the Germano-Lilly [8, 6] dynamic procedure and applied the method for a turbulent channel flow. Bouffanais *et al.* [25] also applied the modal filtering technique in conjunction with the dynamic model in their spectral element method for simulation of a lid-driven cubic cavity flow. Chaudhuri *et al.* [26] applied an adaptive low-pass modal filter to the solution variables to eliminate its high-frequency components and prevent instabilities around the shock.

To the best of our knowledge, the use of a modal filter, with no SGS model, for LES has not been studied in spectral element methods. In this paper, the application of a modal filter in DSEM, without any SGS model, is investigated for LES of isotropic and wall-bounded turbulent flows. A low-pass filter is applied to the primitive variables of the Navier-Stokes equations in the modal space. The performance of such an explicit filter is studied for both decaying isotropic turbulence and a turbulent flow in a periodic channel. Since the filters are applied locally within the elements, the filtering operation is performed on a single processor for each element. This makes the method computationally inexpensive with nearly no impact on the parallelization of the code. Global filters are expensive in spectral element methods [27] due to the necessity for communication between the processors. Since the filtering procedure does not consider any special treatment for the walls, the method can be used for more complex flows.

The remainder of the paper is organized as follows. In section 2, the governing equations and the numerical method are presented. Next, the filtering procedures and formulations are explained in section 3. In section 4, the modal filtering is tested for a problem exhibiting isotropic decaying turbulence, and its performance is compared with two spectral interpolation-based nodal filters. The study continues with the application of the modal filter to LES of a periodic turbulent channel flow. A grid resolution study is performed to ensure grid independence of the method. Furthermore, the ideal choice of the filter strength is investigated by performing simulations using multiple grids with different h and P resolutions. For the channel flow case, an anisotropic version of the modal filter is also introduced and tested. The present methods are also compared in terms of their computational cost. Conclusions are drawn in the last section.

2. Governing Equations and Numerical Methodology

In this section, the governing equations used in the present simulations, as well as the employed numerical method, i.e., the DSEM, are described.

2.1. Governing Equations

The governing equations are the three-dimensional (3D) unsteady Navier-Stokes equations for compressible flows. In DSEM, the governing equations are solved in conservative form. They read

$$\frac{\partial \vec{Q}}{\partial t} + \frac{\partial \vec{F}_i^a}{\partial x_j} = \frac{\partial \vec{F}_i^v}{\partial x_j} \tag{1}$$

in vector notation, where

$$\vec{Q} = \begin{pmatrix} \rho \\ \rho u_1 \\ \rho u_2 \\ \rho u_3 \\ \rho e \end{pmatrix}, \quad \vec{F}_i^a = \begin{pmatrix} \rho u_i \\ p\delta_{i1} + \rho u_1 u_i \\ p\delta_{i2} + \rho u_2 u_i \\ p\delta_{i3} + \rho u_3 u_i \\ u_i(\rho e + p) \end{pmatrix}, \quad \vec{F}_i^v = \begin{pmatrix} 0 \\ \sigma_{i1} \\ \sigma_{i2} \\ \sigma_{i3} \\ -q_i + u_j \sigma_{ij} \end{pmatrix}. \tag{2}$$

In Eq. (1), $\vec{Q}$ is the vector of the conserved variables (solutions), and $\vec{F}_i^a$ and $\vec{F}_i^v$ are the advective and viscous flux vectors, respectively. Also, t is the time, and x_j are the spatial dimensions in the 3D space. In Eq. (2), ρ is the density, u_i are the components of the velocity[1], p is the pressure, and δ_{ij} is the Kronecker delta function. The total energy, viscous stress tensor, and heat flux vector are defined as

$$\rho e = \frac{p}{\gamma - 1} + \frac{1}{2} \rho \, u_i \, u_i \, , \tag{3}$$

$$\sigma_{ij} = \frac{1}{Re_f} \left(\frac{\partial u_i}{\partial x_j} + \frac{\partial u_j}{\partial x_i} - \frac{2}{3} \frac{\partial u_k}{\partial x_k} \delta_{ij} \right) , \tag{4}$$

$$q_i = -\frac{1}{(\gamma - 1) \, Re_f Pr_f M_f^2} \frac{\partial T}{\partial x_i} \, , \tag{5}$$

respectively, where T and γ are the temperature and the heat capacity ratio, respectively. The reference Reynolds number, reference Prandtl number, and reference Mach number are defined as

$$Re_f = \frac{\rho_f^* l_f^* u_f^*}{\mu^*}, \quad Pr_f = \frac{c_p^* \mu^*}{k^*}, \quad M_f = \frac{u_f^*}{c_f^*}, \tag{6}$$

respectively. In Eq. (6), ρ_f^*, l_f^*, and u_f^* are the reference density, reference length, and reference velocity, respectively, and μ^* is the fluid's dynamic viscosity. Variables with superscript $*$ are dimensional variables. Also, k^* and c_p^* are the thermal conductivity coefficient and the fluid's constant pressure specific heat, respectively, and $c_f^* = \sqrt{\gamma R^* T_f^*}$ is the reference speed of sound based on the reference temperature, T_f^*, where R^* is the gas constant. The ideal gas equation of state in non-dimensional form, given by $p = \rho T / \gamma M_f^2$, closes the governing equations.

2.2. Numerical Methodology

A nodal collocation form [28] of the DSEM [29, 30] is used in this work. Spectral element methods combine the exponential convergence of spectral methods and the geometric flexibility of finite element methods. DSEM introduces negligible diffusion and dispersion errors and is spectrally convergent for smooth solutions within each element [29, 30]. It also offers useful features such as efficient parallelization and the ability to locally refine the grid either by increasing the number of elements (h-refinement) or by increasing the polynomial order (p-refinement). The method has been tested for direct numerical simulation (DNS) and LES of compressible turbulent flows in complex geometries [31, 32, 33, 34, 35]. The DSEM solves the governing equations of compressible flows and allows for discontinuity of the solution on interfaces between the elements.

In DSEM, the 3D physical domain is divided into a finite number of non-overlapping arbitrary shaped hexahedral subdomains, so-called elements. Each element is then transformed to a unit cube, called the mapped space, using an iso-parametric mapping. In the mapped space, the governing equations, Eq. (1), read

$$\frac{\partial \widetilde{Q}}{\partial t} + \frac{\partial \widetilde{F}_i^a}{\partial X_j} = \frac{\partial \widetilde{F}_i^v}{\partial X_j} \, , \tag{7}$$

[1] For convenience, $[u_1, u_2, u_3]$ and $[u, v, w]$ are interchangeably used for the streamwise (x_1 or x), normal (x_2 or y), and spanwise (x_3 or z) components of the velocity, respectively.

with

$$\widetilde{Q} = J\vec{Q}\,; \quad \widetilde{F}_i^a = \frac{\partial X_i}{\partial x_j}\vec{F}_j^a\,; \quad \widetilde{F}_i^v = \frac{\partial X_i}{\partial x_j}\vec{F}_j^v\,. \tag{8}$$

In Eqs. (7)-(8), the tilde denotes a mapped vector, and J is the Jacobian of the mapping [28]. Also, X_j are the spatial dimensions in the mapped space, as opposed to x_j, which are the spatial dimensions in the physical space. Within each element, the spectral method is applied on a staggered Chebyshev grid [29]. The staggered grid in a one-dimensional (1D) element consists of the Gauss collocation points for calculation of the solution values, and Gauss-Lobatto collocation points for calculation of the fluxes. The distributions of the Gauss points and the Gauss-Lobatto points in the mapped space on the interval $[0, 1]$ are given by

$$X_{i+\frac{1}{2}} = \frac{1}{2}\left[1 - \cos\left(\frac{i+\frac{1}{2}}{p+1}\,\pi\right)\right], \quad i = 0, \ldots, p\,, \tag{9}$$

and

$$X_i = \frac{1}{2}\left[1 - \cos\left(\frac{i}{p+1}\,\pi\right)\right], \quad i = 0, \ldots, p+1, \tag{10}$$

respectively, where P is the polynomial order. In the two-dimensional (2D) version, the staggered grid consists of Gauss-Gauss (GG) points for the solution values and Lobatto-Gauss (LG) and Gauss-Lobatto (GL) points for the fluxes in the x- and y-directions, respectively. The distribution of points of a 2D element obeys the same formulation as the 1D element in each direction. An example of such a 2D staggered grid with polynomial order $P = 2$ is depicted in Fig. 2. Similarly, a 3D staggered grid consists of GGG points for the solution and LGG, GLG, and GGL points for

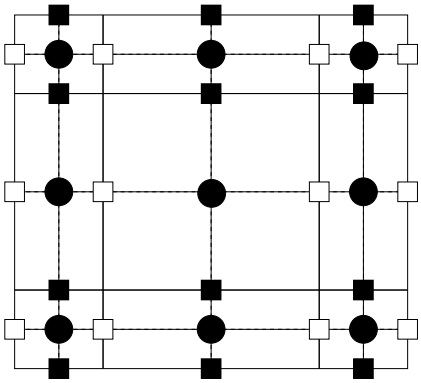

Fig. 2: The staggered grid for a 2D element with polynomial order $P = 2$. Closed circles: Gauss-Gauss (GG) points, open square: Lobatto-Gauss (LG) points, closed square: Gauss-Lobatto (GL) points.

the fluxes. The solution at any point within a 3D element in the mapped space is approximated by

$$\widetilde{Q}(X, Y, Z) = \sum_{i=0}^{p}\sum_{j=0}^{p}\sum_{k=0}^{p} h_{i+\frac{1}{2}}(X)\; h_{j+\frac{1}{2}}(Y)\; h_{k+\frac{1}{2}}(Z)\; \widetilde{Q}_{i+\frac{1}{2},j+\frac{1}{2},k+\frac{1}{2}}\,, \tag{11}$$

where $\widetilde{Q}_{i+\frac{1}{2},j+\frac{1}{2},k+\frac{1}{2}}$ is the solution value at the GGG points, and $h_{i+1/2}$ is the Lagrange interpolating polynomial calculated on the GGG grid. The advective and viscous fluxes are calculated at every time step. The fluxes are patched at the interfaces of the elements by the so-called mortar method to achieve C^0 continuity of the flux values [28]. The time integration is performed using a fourth-order, low-storage Runge-Kutta scheme [28].

3. Filtering Procedures

Two filtering procedures are presented in this work. A filtering procedure in a spectral element method can be constructed using either a modal low-pass filter in the modal space or an interpolant-projection in the nodal space [24]. For the case of modal filtering, the solution needs to be transformed from the nodal representation to the modal representation within each element. Then, the modes with the highest frequencies are set to zero. Finally, the modes

are transformed back to the nodal space. For the case of a nodal filter, the solution, which is constructed as a sum of basis functions of order P in each element, is interpolated to a basis function of order P', where $P' < P$. Then, the solution is projected back to the original basis function of order P. Though the two filters introduced here are designed to remove high-frequency motions of the flow, they are different than conventional filters in terms of their operating mechanism to achieve the same goal; they may be considered as projection operators instead. The two filtering approaches are explained in detail in the following sections.

3.1. Modal Filter

A solution function in a spectral element method can be expressed in either nodal or modal representation. In the nodal representation, the function is expressed through the values of the function on a set of specific points in space. In the modal representation, the function is expressed through the coefficients of a set of orthogonal expansion functions, or modes. The two representations are mathematically equivalent, but each has its own computational properties [36]. A local solution function, $\tilde{u}(X,t)$, inside a 1D element with a polynomial order of P in the mapped space can be expressed at a specific time via its modal expansion as

$$\tilde{u}(X) = \sum_{k=0}^{P} \hat{u}_k \, \psi_k(X), \tag{12}$$

where $\psi_k(X)$ are the basis functions, and $\hat{u}_k$ are the expansion coefficients. The basis functions form a hierarchical set, i.e., each successive mode represents motions with higher spatial frequencies. In the modal filtering approach, the solution variables are transformed from the nodal to the modal representation, and the expansion coefficients that correspond to the highest frequencies are set to zero. The transformation mechanism between the nodal representation, $\tilde{u}(X)$, and the modal representation, $\hat{u}_k$, of the solution is a discrete Chebyshev transform (DChT) [37],

$$\hat{u}_k = \frac{2}{N} \sum_{i=0}^{N-1} \tilde{u}(X_{i+\frac{1}{2}}) \cos\left[\frac{k\pi}{N}\Big(i+\frac{1}{2}\Big)\right], \quad k = 0, \ldots, N-1, \tag{13}$$

and an inverse discrete Chebyshev transform (iDChT),

$$\tilde{u}(X_{i+\frac{1}{2}}) = \frac{1}{2}\,\hat{u}_0 + \sum_{k=1}^{N-1} \hat{u}_k \cos\left[\frac{k\pi}{N}\Big(i+\frac{1}{2}\Big)\right], \quad i = 0, \ldots, N-1. \tag{14}$$

Both transformations are implemented in DSEM using the library *Fastest Fourier Transform in the West* (FFTW) [38]. The three-dimensional variations of DChT and its inverse are simply separable products of the one-dimensional definitions along each dimension and are also provided by FFTW.

The expansion functions in multiple space dimensions are the tensor-products of the 1D functions, and the filtering procedure in three dimensions is applied using the matrix tensor product properties. Assume $\tilde{u}(X,Y,Z)$ is the solution in the mapped nodal space within a 3D element with a polynomial order of P. The solution function can be expressed via its modal expansion as

$$\tilde{u}(X,Y,Z) = \sum_{k=0}^{P} \sum_{l=0}^{P} \sum_{m=0}^{P} \hat{u}_{klm} \, \psi_k(X)\psi_l(Y)\psi_m(Z), \tag{15}$$

where $\hat{u}_{klm}$ are the 3D expansion coefficients, which represent the modes of the function in the 3D space; therefore, we call it the modal matrix. An example of such a 3D matrix is shown in Fig. 3(a) for a polynomial order of $P = 8$. Each small cube represents an entry of the modal matrix, i.e., an expansion coefficient. After transforming the solution to the modal space, we can modify the modes as desired, and then return the solution to the nodal space using an iDChT. The component $\hat{u}_{000}$ of the modal matrix represents the bulk value of the function within the element (Fig. 3(b)), while components $\hat{u}_{k00}$, $\hat{u}_{0l0}$, and $\hat{u}_{00m}$ represent the modes purely in the x-, y-, and z-directions, respectively (Fig. 3(c)). Consequently, components with combinatory subscript represent the combinatory modes in the 3D space. Also, the components with lower subscript represent the low-frequency modes, and the components with higher subscript represent the high-frequency modes. Therefore, lowering the values of the components with higher subscript is equivalent to damping the high-frequency motions, which is the aim here. For example, if we set all the components $\hat{u}_{klm}$, where $\max\{k,l,m\} = P$, to zero, it is equivalent to removing all the motions with contributions from

the highest-frequency modes from at least one direction. There are $3P^2+3P+1$ such components, and they are shown in Fig. 3(d) for $P = 8$. Therefore, applying a modal low-pass filter with modal strength N_f means (i) transforming the solution from the nodal to the modal space via DChT, given by Eq. (13), (ii) removing all combinatory modes that have contributions from the N_f highest-frequency spatial modes in any direction, i.e.,

$$\hat{u}_{klm} = 0 \quad \forall \quad \{k,l,m\} \quad \text{where} \quad \max\{k,l,m\} > P - N_f, \tag{16}$$

and (iii) transforming the solution back to the nodal space via iDChT, given by Eq. (13). For example, for $N_f = 2$, the entries that are removed, i.e., set to zero, are those shown in Fig. 3(e). We call this filtering operation isotropic modal filtering since the higher-frequency modes are removed from all three directions.

Alternatively, setting components $\hat{u}_{klm}$, where for example $k = P$, to zero is equivalent to removing all motions with any contribution from the highest-frequency modes in the x-direction. There are $(P+1)^2$ such components, and they are shown in Fig. 3(f) for $P = 8$. Therefore, applying a modal low-pass filter with strength N_f in the ith direction means (i) transforming the solution from the nodal to the modal space by applying the DChT, given by Eq. (13), (ii) removing all combinatory modes that have contributions from the N_f highest-frequency modes in the i-direction, i.e.,

$$\hat{u}_{klm} = 0 \quad \forall \quad \{k,l,m\} \quad \text{where} \begin{cases} k > P - N_f & (x\text{-direction}) \\ l > P - N_f & (y\text{-direction}) \\ m > P - N_f & (z\text{-direction}) \end{cases}, \tag{17}$$

for removing the high-frequency modes in the x-, y-, or z-directions, respectively, and (iii) transforming the solution back to the nodal space via the iDChT, given by Eq. (14). We call this filtering operation anisotropic modal filtering since the higher-frequency motions are removed only from specific directions. The anisotropic version of the modal filter is tested for the non-isotropic case, i.e. the turbulent channel flow.

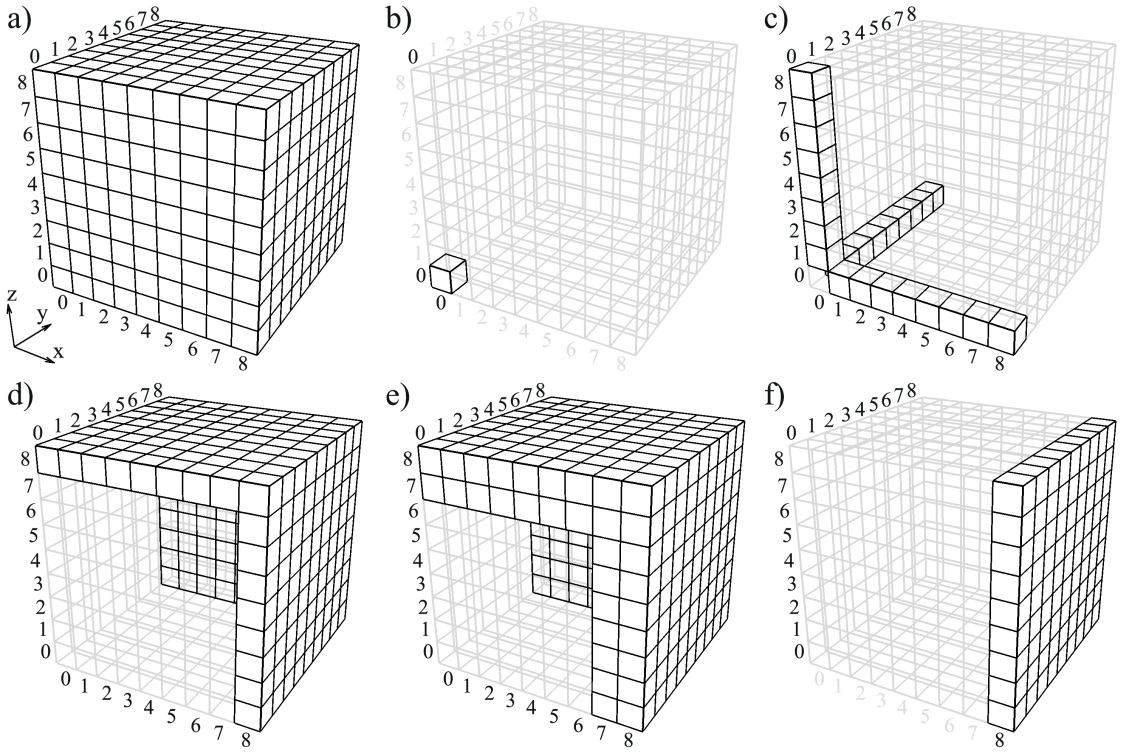

Fig. 3: Modal matrix for an element with polynomial order of $P = 8$: (a) the complete matrix; (b) the zeroth mode, $\hat{u}_{000}$; (c) modes purely in the x-, y-, or z-directions, $\hat{u}_{k00}$, $\hat{u}_{0l0}$, and $\hat{u}_{00m}$; (d) highest-frequency modes in all three directions; (e) two highest-frequency modes in all three directions; (f) highest-frequency modes in the x-direction.

3.2. Nodal Filter

The second filtering method is called nodal filtering [25, 27]. In this method, the filtered values of a variable in an element with a polynomial order of P are obtained by interpolating the variable to a grid with a lower polynomial order of $P' < P$, then projecting the solution back onto the original grid with the polynomial order of P [25]. The nodal filter is also called an interpolant-projection filter [24, 19] or interpolation-based filter [17, 39]. The nodal filtering procedure is expected to dampen high-frequency oscillations that have contributions from the N'_f highest-frequency modes in three directions, where $N'_f = P - P'$ is the filter strength [25]. This is due to the fact that the basis with the lower order, P', does not have the capacity to capture the spatial modes corresponding to the N'_f highest-frequency modes. Note that for the modal filter, N_f is defined as the number of high-frequency modes that are explicitly removed from the modal space, while for the nodal filter, N'_f is defined as the difference between the order of the two polynomial space ($P - P'$). Both variables indicate the number of high-frequency modes intended to be removed and represent the strength of the filters.

To formulate the nodal filter, first, we look at the procedure for a 1D element. The interpolation and projection could be applied to both nodal sets, Gauss-Gauss and Gauss-Lobatto nodes. Here, we apply the filter on the Gauss-Lobatto nodal set since it preserves the endpoint values of the original function. The first step is to interpolate the original function from a polynomial of degree P to a polynomial of lower degree P' by

$$\widetilde{Q}'\left(X'_i\right) = \sum_{j=0}^{P} h_j\left(X'_i\right)\ \widetilde{Q}(X_j). \tag{18}$$

where X_j and $\widetilde{Q}$ are the grid points and the solution values on the original (P) polynomial space, respectively, while primed variables are the same entities on the secondary (P') polynomial spaces. The interpolation can be expressed as matrix-vector product by [19]

$$\widetilde{Q}'_i = I^{\text{int}}_{ij}\ \widetilde{Q}_j, \tag{19}$$

where

$$I^{\text{int}}_{ij} = \prod_{k=0,k\neq j}^{P} \frac{X'_i - X_k}{X_j - X_k}, \quad i = 0,\ldots,P', \quad j = 0,\ldots,P, \tag{20}$$

is the interpolation matrix. The second step is projecting the function $\widetilde{Q}'\left(X'\right)$ back to the polynomial space P, resulting the filtered function,

$$\widetilde{Q}^{\text{filt}}(X_j) = \sum_{i=0}^{P'} h_i\left(X_j\right)\ Q'(X'_i). \tag{21}$$

Similarly, the second operation can be expressed as a matrix-vector form by [19]

$$\widetilde{Q}^{\text{filt}}_j = I^{\text{pro}}_{ji}\ \widetilde{Q}'_i, \tag{22}$$

with the projection matrix, I^{pro}_{ji} defined by

$$I^{\text{pro}}_{ji} = \prod_{k=0,k\neq i}^{P'} \frac{X_j - X'_k}{X'_i - X'_k}, \quad j = 0,\ldots,P, \quad i = 0,\ldots,P'. \tag{23}$$

There are two approaches to extend the 1D interpolation and projection procedures described in Eqs. (18) and (21) to 3D space. The first approach is to apply the 1D procedure to all 1D arrays in the x-direction, then in the y-direction, and then in the z-direction. We call this approach, which is used in previous work [15, 19], a series nodal filter. The alternative approach is to generalize Eqs. (18) and (21) for 3D space as

$$\widetilde{Q}'(X'_l, Y'_m, Z'_n) = \sum_{i=0}^{P}\sum_{j=0}^{P}\sum_{k=0}^{P} h_i(X'_l)h_j(Y'_m)h_k(Z'_n)\ Q(X_i, Y_j, Z_k) \tag{24}$$

and

$$\widetilde{Q}^{\text{filt}}(X_i, Y_j, Z_k) = \sum_{l=0}^{P'}\sum_{m=0}^{P'}\sum_{n=0}^{P'} h_l(X_i)h_m(Y_j)h_n(Z_k)\ \widetilde{Q}'(X'_l, Y'_m, Z'_n). \tag{25}$$

In this approach, which we call a 3D nodal filter, the interpolation and projection defined in Eqs. (24) and (25) are sequentially applied to the variables in all 3D elements.

4. Isotropic Decaying Turbulence

The results for LES of a 3D isotropic decaying turbulence are presented in this section. The aim is to assess the performance of the filters for an isotropic turbulence condition. Different filtering techniques, including the modal filter and two nodal filters, are tested, and the results are compared with DNS and no-model coarse DNS.

4.1. Problem Setup

The problem setup is similar to the isotropic turbulence of Blaisdell *et al.* [40]. The simulation is performed in a cube with periodic boundary conditions in three directions. The length of the cube is 2π units in each direction. The domain is divided into six uniformly distributed elements in each direction, resulting in a total of 216 elements. A polynomial order of $P = 8$ is used for the basis functions within each of the elements. The total number of solution (Gauss) points is $N_p = 6^3 \times (8+1)^3 = 157{,}464$.

An initial condition should be specified such that it generates an isotropic and periodic field for the velocity and thermodynamic variables. The procedure outlined by Blaisdell *et al.* [40] for the case "idc96" is followed here to initialize the solution domain. The domain is initialized by a correlated turbulent flow field using a specified initial energy spectra. The spectra follow a top-hat distribution that has non-zero contributions in the wavenumber range of $8 \leq k \leq 16$. In this work, a divergence-free initial field is considered for the thermodynamic variables; therefore, only the mean values of density, pressure, and temperature are specified. The initial velocity fluctuations are purely solenoidal and exist in all three directions. The initial field is first obtained on a uniform grid from the Fourier coefficients using a fast Fourier transform. The field is then interpolated from the Fourier grid to the Gauss grid points.

The bulk rms velocity at a fixed time instant is defined as

$$u_{\text{rms}} = \sqrt{\frac{\overline{u_i u_i}}{3}}, \tag{26}$$

where the overline denotes a spatial average over the whole domain. Turbulence kinetic energy (TKE) is defined as the integral of the energy spectrum function, $E(k)$, over all wavenumbers,

$$\text{TKE} = \int_0^\infty E(k)\, dk = \frac{1}{2}\,\overline{u_i u_i}. \tag{27}$$

4.2. Results

The results of applying different filtering procedures on the isotropic turbulence are presented in this section. First, the filters are applied once to the initial field before running the simulation to study the direct effect of the filters on a turbulence field (a priori analysis). Then, the decaying isotropic turbulence is simulated using different filtering approaches, and the performance of the filters in the prediction of the flow statistics are compared (a posteriori analysis).

4.2.1. A Priori Analysis

In this section, the effects of the isotropic modal filter and both series and 3D nodal filters on an isotropic turbulence field are considered. The filters are applied one time to a 3D isotropic turbulence field, and the solution fields before and after applying the filter are compared. The turbulence field is obtained by running the isotropic turbulence case described above for a duration of $t = 1$ without applying any filter.

First, we apply the filters on the 3D isotropic turbulence field and examine the solution values on a 1D sample line across the domain. Figure 4(a)-(c) shows the u-velocity along a 1D sample line across the domain from the original field and filtered fields obtained from different filtering procedures with different strengths. By applying a stronger filter (larger N_f and N'_f) at each step, the solution is expected to become smoother, and the high-frequency features of the signal are expected to weaken. With the modal filtering (Fig. 4(a)), it is observed that the solution becomes smoother with each consecutive step, where more high-frequency modes are removed. With the nodal filters, however, this behavior is observed only for weaker filters ($N'_f < 3$). Applying stronger nodal filters appears to introduce inconsistent contributions to the motions, and change the general shape of the function. Such behavior can be seen in $1 < x < 2$ for $N'_f = 4$ and 5 for both nodal filters and more clearly in $2.3 < x < 3.3$ for the series nodal filter. This means that by applying stronger nodal filters to the flow variables, non-physical effects are superimposed

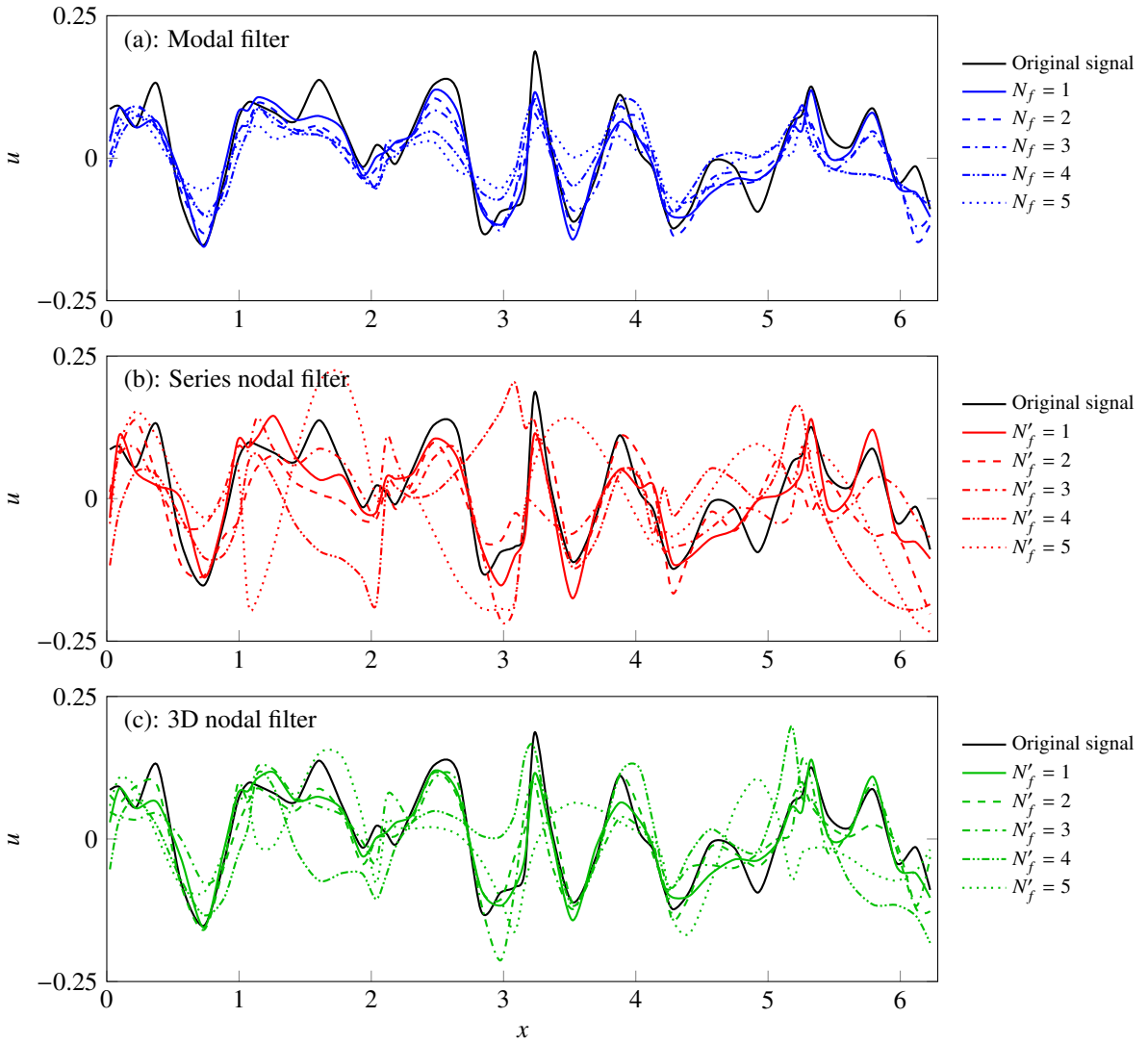

Fig. 4: The effect of (a) the modal filtering, (b) series nodal filtering, and (c) 3D nodal filtering on a 1D signal. The signal is the u-velocity on a sample line through the isotropic turbulence field.

on the lower-frequency motions that could result in incorrect turbulence statistics. This low-frequency effect appears to be stronger for the series nodal filter than the 3D nodal filter. Note that a nodal filter with $N'_f = 4$ or 5 might be too strong for a practical case of LES; however, visualizing their results help magnify the effects to better understand their differences with modal filtering.

Following the results obtained from a 1D sample signal across the domain, further investigation of the effect of the nodal filter on the modes of the solution is performed. This time, the nodal filter is applied once to all variables in all elements for the same isotropic turbulence field at time $t = 1$, and the average properties among all elements before and after applying the filter are compared (shown later). The amplitude of modes with wavenumber n in element q before applying the filter is defined by

$$A_q(n) = \langle \hat{u}_{klm} \rangle \quad \forall \quad \{k,l,m\} \quad \text{where} \quad \max\{k,l,m\} = n, \quad n = 0,\ldots,P, \tag{28}$$

where $\langle\rangle$ means the average of the set. Examples of these sets are shown in Fig. 5 for $n = 6$, 7, and 8. Similarly, the amplitude of modes with wavenumber n in an element after applying the filter is called $A_q^{\text{filt}}(n)$.

The procedure used to study the effects of filters on the modes is as follows. First, we transform the solutions from nodal representation to modal representation via DChT, given by Eq. (13), and store the amplitudes of the modes (Eq.

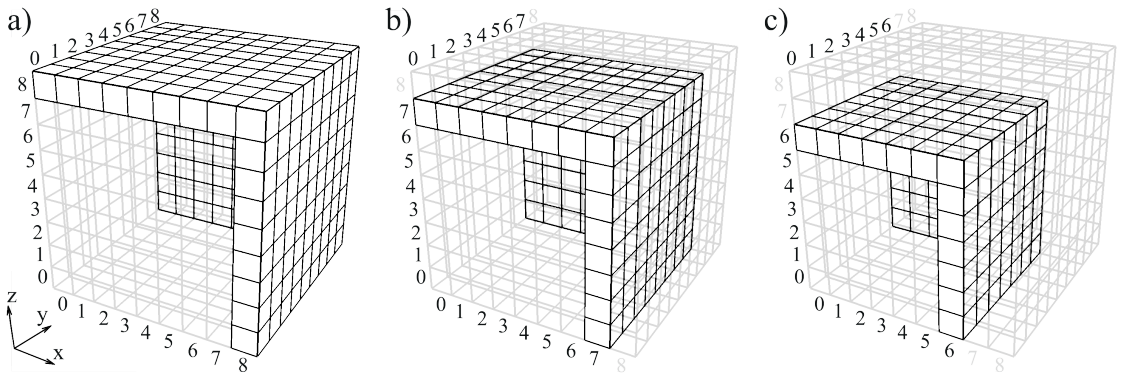

Fig. 5: The entries of the modal matrix that contribute to motions with wavenumber n for (a) $n = 8$, (b) $n = 7$, and (c) $n = 6$.

(28)). Then, we apply the filter of interest on the variables of interest and transform the filtered solutions from nodal representation to modal representation. Finally, we compare the amplitude of the filtered modes ($A_q^{\text{filt}}(n)$) with the previously stored original modes ($A_q(n)$). This procedure is used for the nodal filters. The effect of the modal filter on the modes is trivial.

After calculating $A_q(n)$ and $A_q^{\text{filt}}(n)$ for all the elements, the amplitude of each wavenumber is averaged for all the elements throughout the domain to obtain $\langle A(n)\rangle$ and $\langle A^{\text{filt}}(n)\rangle$. Here, we are interested in the effect of the nodal filter on the amplitudes of modes at different wavenumbers. Therefore, for each wavenumber, we look at the amplitude of each wavenumber after applying the filter, relative to the amplitude of the same wavenumber before applying the filter: $\widetilde{A}(n) = \langle A^{\text{filt}}(n)\rangle / \langle A(n)\rangle$. This study identifies the statistical effect of the filters on the amplitude of each wavenumber. An ideal filter would remove the high wavenumbers, and at the same time will not affect the low wavenumbers.

Figure 6(a) shows the relative amplitudes of modes ($\widetilde{A}(n)$) at each wavenumber (n) after applying the modal filter with different strengths (N_f). The motions are calculated based on u-velocity. Note that even though some adjacent points are connected with a sloped line, they do not represent smooth transitions, but a sharp cutoff, i.e., the relative amplitudes of the modes are one and zero for two adjacent wavenumbers. Not surprisingly, it is observed that by applying a modal filter, the last N_f modes with the highest frequencies are completely removed, and the relative amplitude of the lower-frequency modes remain as one, which means those modes are not affected by the filtering procedure.

Figures 6(b) and (c) show the effect of series and 3D nodal filters on the u-velocity modes, respectively. By interpolating the solutions back and forth to a lower polynomial order, $P' = P - N_f'$, the motions associated with the N_f' modes with highest frequencies are expected to be completely removed with no effect on the other modes with lower frequencies. From Fig. 6(b) it is observed that by applying the series nodal filter with $N_f' = 1$, the mode with the highest frequency ($n = 8$) is completely removed. However, the process has some weak effects on the lower-frequency modes as well—two adjacent modes, i.e., $n = 6$ and 7, are slightly amplified. The amplification of modes is not expected from a low-pass filter, where the modes should be removed or weakened. This effect could increase the motions at unintended scales and contaminate the flow statistics. For $N_f' = 2$, the two modes with the highest frequencies ($n = 7$ and 8) are completely removed. However, again, some of the lower-frequency modes are also affected. This time, three adjacent modes ($n = 4$, 5, and 6) are altered. Similarly, for $N_f' = 3$, four adjacent modes are affected. This low-frequency effect dramatically escalates for $N_f' > 3$ such that the filtering process significantly changes the lowest-frequency modes. The value of $\widetilde{A}(n)$ at three low-frequency end of the spectra, i.e., $n = \{0, 1, 2\}$, mostly fall outside the plot frame and are given by $\widetilde{A}(n) = \{-0.34, 2.72, 3.24\}$ and $\{3.29, 3.97, 0.39\}$ for $N_f' = 4$ and 5, respectively. This observation conveys that the series nodal filter, especially at higher strengths, provokes significant contributions to the low-frequency motions and is consistent with the observation in Fig. 4(b), where the general shape of the function changes for $N_f' > 3$. This unintended contamination of the low-frequency motions may remove more turbulent motions than what is intended and severely affect the first-, as well as second-order statistics.

A less severe version of the above-mentioned low-frequency effect is also observed in the 3D nodal filter, shown in Fig 6(c). The 3D nodal filter acts similar to the modal filter, i.e., the filtering procedure does not affect the lower-frequency modes, only for $N_f' = 1$. For higher values of N_f', the low-frequency effect is present, but, compared with the series nodal filter, fewer adjacent modes are changed at a lower rate. The low-frequency effect becomes severe for

$N'_f = 5$; the points $\widetilde{A}(0) = 3.65$ and $\widetilde{A}(2) = -1.36$ for $N'_f = 5$ fall outside the plot frame. This is a new observation and shows that the nodal filter accomplishes one of the two expected goals: It does remove the motions within a certain frequency range, but it does not leave the lower-frequency motions unaffected.

4.2.2. A Posteriori Analysis

LES of the isotropic decaying turbulence case is conducted using different filtering procedures to compare their performance. A DNS of the same flow is also simulated as the benchmark. Turbulence statistics such as the decay of the TKE, the energy spectra, and the dissipation spectra are used for comparison. The filters are applied to density, three components of velocity, and pressure at each time step. The initial turbulent Mach number based on u_{rms} is $M_{T,0} = 0.3$, and the initial Taylor Reynolds number is $Re_\lambda = 40$. More details of the problem setup are given in Sengupta [19].

The grid used for DNS consists of $6^3 = 216$ elements, uniformly distributed in three directions. The polynomial order used for DNS is $P = 15$. This grid has been shown to be sufficiently fine for DNS of the described isotropic turbulence case [19]. The elements of the grid used for LES are the same as those used for DNS; however, the polynomial order for LES is $P = 8$ as opposed to $P = 15$. A coarse DNS case is also simulated using the low polynomial of LES without applying a turbulence model.

Figure 7(a) and (b) show the energy spectra and the dissipation spectra, respectively, of the isotropic decaying turbulence simulation at time $t = 3.2$ for the DNS and coarse DNS cases. The energy spectrum is compared with previously published data of Blaisdell *et al.* [41]. A good agreement with previous data is observed for the DNS case. The sharp drop-off in the spectrum at high wavenumbers indicates a resolved DNS. The work of Blaisdell *et al.* [41] used a Fourier-spectral method with $96^3 = 884{,}736$ grid points. The present DNS grid has the same number of degrees of freedom as the previous work with $216 \times 16^3 = 884{,}736$ Gauss grid points. This conclusion is consistent with the validation study of Jacobs *et al.* [42]. On the other hand, the coarse DNS case is unable to capture the expected drop-off in both energy and dissipation spectra for $k > 13$.

Figure 8(a)-(c) shows the energy spectra of the isotropic decaying turbulence using the three different filtering approaches. The spectra are compared with the results obtained from DNS and coarse DNS cases. All three methods provide steeper drop-off than the coarse DNS case at high wavenumbers, which is expected. It means that the filters are serving as a drain for the turbulence energy cascade. Except for the 3D nodal filter, removing two modes results in a steeper drop-off than removing one mode; a stronger filter damps more energy from the high wavenumber portion of the spectrum. For the nodal filters, the spectra are affected at midrange wavenumbers (for both nodal filters) and low wavenumbers (for series nodal filter). This undesired side effect could induce non-physical contributions to the larger-scale motions of the turbulence and result in incorrect turbulence statistics. This behavior is not expected since a low-pass filter ideally acts on the high wavenumbers only. The best agreement with DNS is obtained by removing one mode using the modal filter.

The decay of the TKE, defined by Eq. (27), for the isotropic decaying turbulence is shown in Fig. 9(a)-(c) for the modal filtering, the series nodal filtering, and the 3D nodal filtering procedures, respectively. The results are compared with DNS. It is observed that the TKE has a noticeable deviation from DNS for the series nodal filter, with $N'_f = 1$ and 2, for $t > 1$. The 3D nodal filter, with $N'_f = 2$, also overpredicts the TKE from the beginning of the simulation ($t = 0$). The nodal filters generally predict a lower rate of decay of the TKE compared to the DNS case. The modal filtering, for both filter strengths $N_f = 1$ and 2, provides good agreement with the DNS.

It is observed from the simulations of the isotropic turbulence that the nodal filtering not only drastically alters the low-frequency content, but amplifies the lower modes due to $|\widetilde{A}(n)| > 1$ and introduces large phase shifts due to negative values of $\widetilde{A}(n)$. The consequence of this observation is clearly demonstrated in Fig. 8, where the energy of LES cases are considerably higher than DNS, which in reality should be the opposite. This phenomenon is due to the aliasing inherent in the interpolation-based operations, Eqs. (24) and (25), which causes the redistribution of energy between modes. Based on the above-mentioned observations, it is strongly recommended to avoid using the nodal explicit filter for LES. Therefore, the modal filter is used for further LES of turbulent channel flow in this work.

5. Channel Flow

The periodic turbulent channel flow between two parallel plates is a well-studied benchmark for turbulence models [2, 3, 16, 24, 43]. It provides a simple flow that assesses the performance of turbulence models near the wall. The tests with isotropic decaying turbulence, presented in the previous section, demonstrated the superior performance

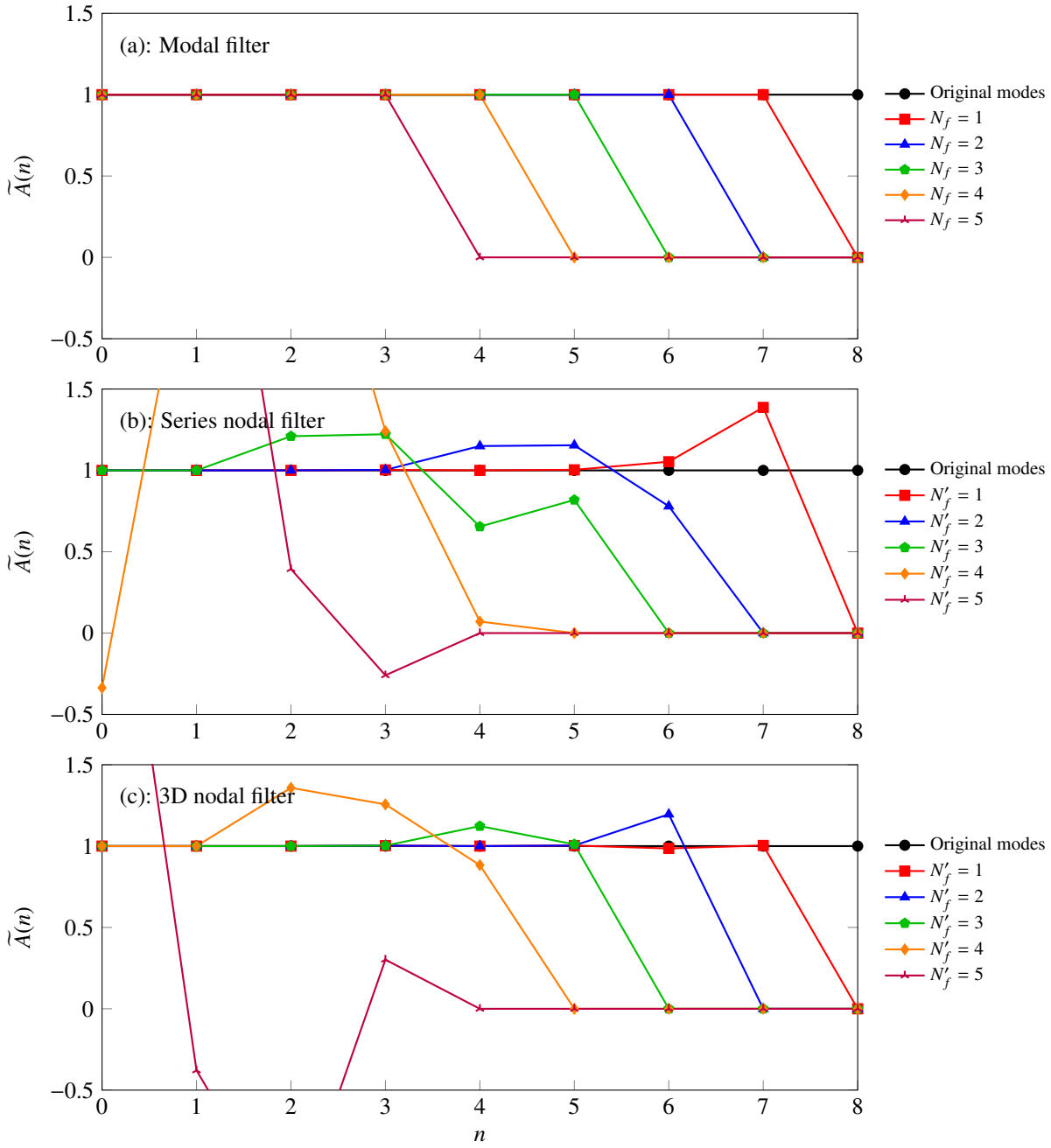

Fig. 6: The effect of (a) the modal filtering, (b) series nodal filtering, and (c) 3D nodal filtering on the magnitude of motions corresponding to different modes. The motions are u-velocity throughout the domain.

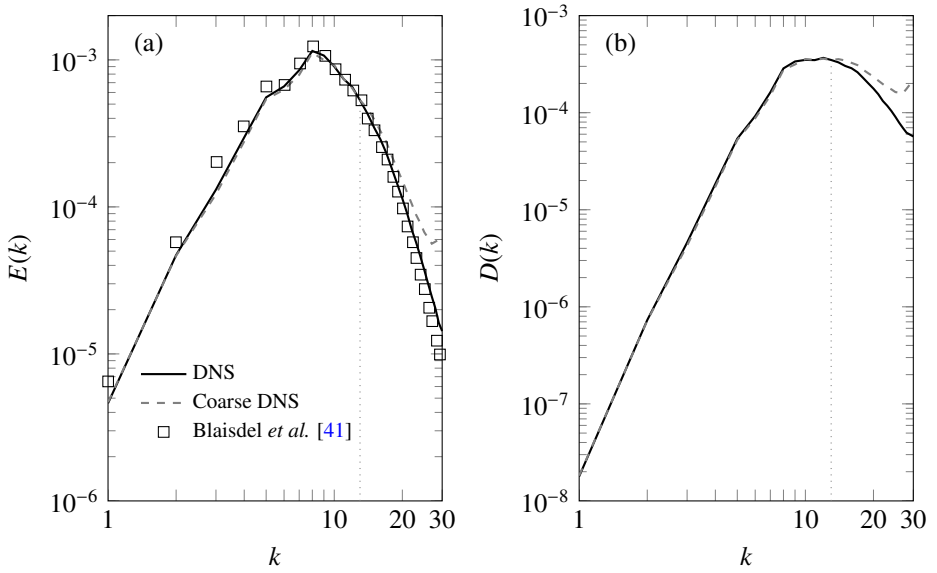

Fig. 7: (a) The energy spectra and (b) dissipation spectra for the isotropic decaying turbulence at time $t = 3.2$.

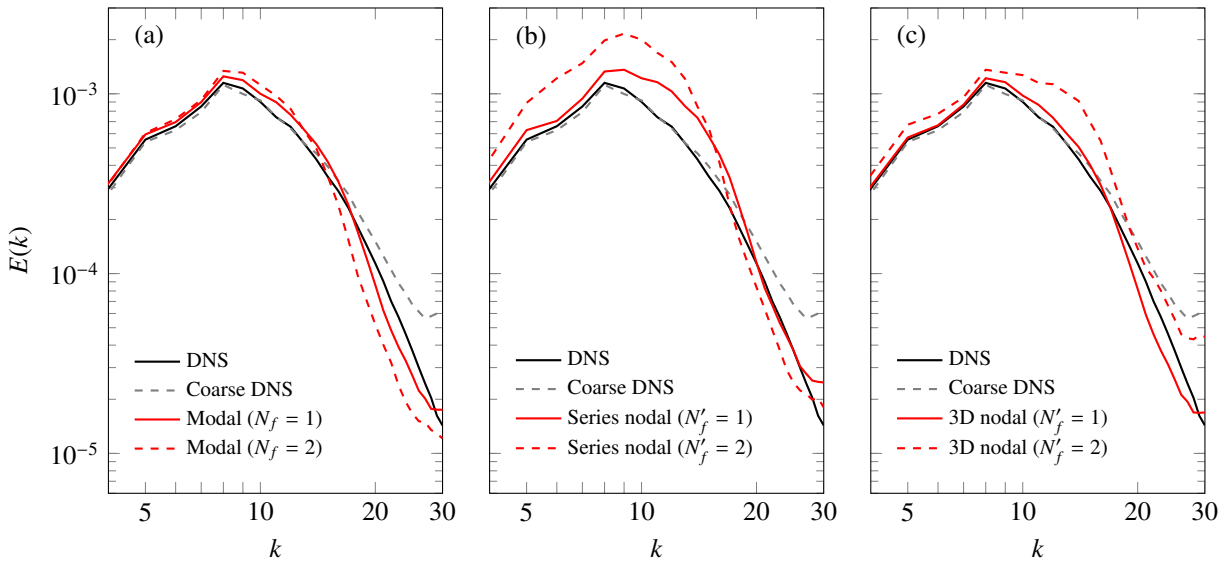

Fig. 8: The energy spectra of the isotropic decaying turbulence at time $t = 3.2$ for (a) the modal filter, (b) series nodal filter, and (c) 3D nodal filter as compared with DNS and coarse DNS.

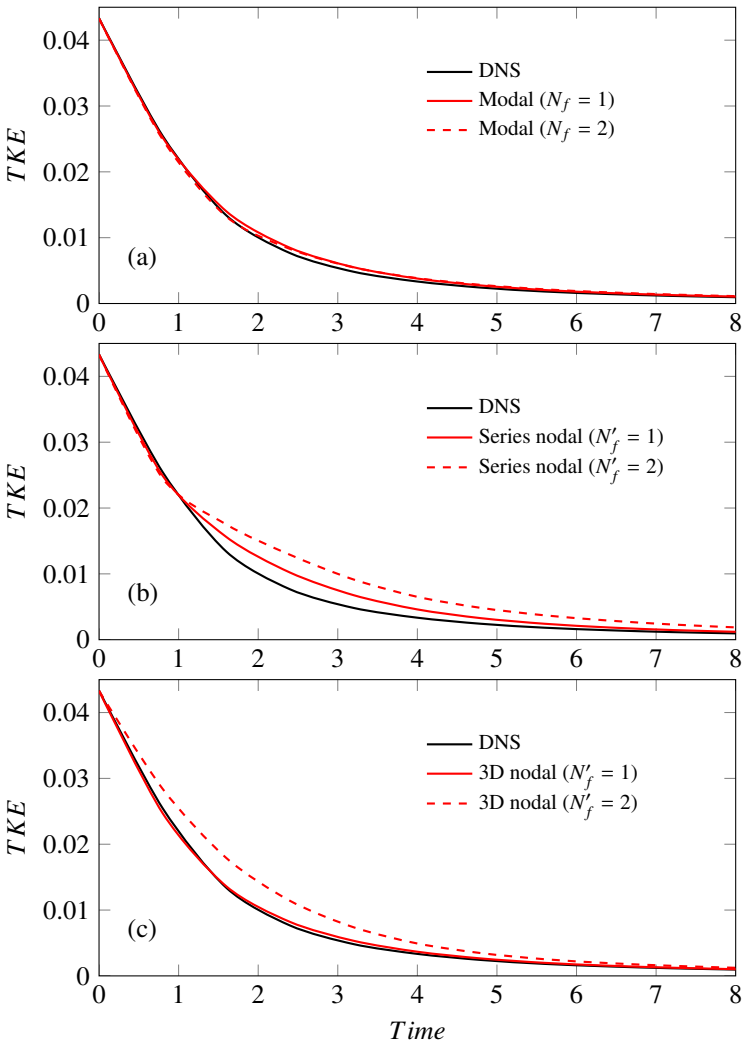

Fig. 9: Evolution of the turbulent kinetic energy (TKE) for (a) the modal filter, (b) series nodal filter, and (c) 3D nodal filter, compared with DNS.

of the modal filter over the nodal filters. Therefore, for further simulations of channel flow, only the modal filtering procedure is employed.

5.1. Problem Setup

In the present work, we perform LES of a 3D periodic turbulent channel flow to study the performance of the modal filtering procedure in the case of wall-bounded turbulence. First- and second-order turbulent statistics are used to assess the accuracy of the calculations. The DNS of Lee and Moser [44] at the friction Reynolds number of $Re_\tau = 544$ is used as the reference.

5.1.1. Computational Domain

The channel flow configuration is shown in Fig. 10. The flow runs between two parallel no-slip isothermal walls with a temperature of $T_w = 1$, which are placed in the xz-plane. The boundaries of the domain in the streamwise (x) and spanwise (z) directions are periodic. The dimensions of the computational domain are $L_x = 4\pi$, $L_y = 2$, and $L_z = 2\pi$ in the streamwise, wall-normal, and spanwise directions, respectively. All lengths are scaled by the channel's half-height, $\delta = L_y/2$. The domain dimensions in terms of the wall unit are $L_x^+ \approx 6{,}800$, $L_y^+ \approx 1{,}100$, and $L_z^+ \approx 3{,}400$. Throughout the paper, variables with the superscript $^+$ are scaled by wall units. These channel dimensions are used in previous DNS [45], and are shown to be sufficiently large to encompass the largest scale of turbulence by demonstrating two-point correlations in the periodic directions [46].

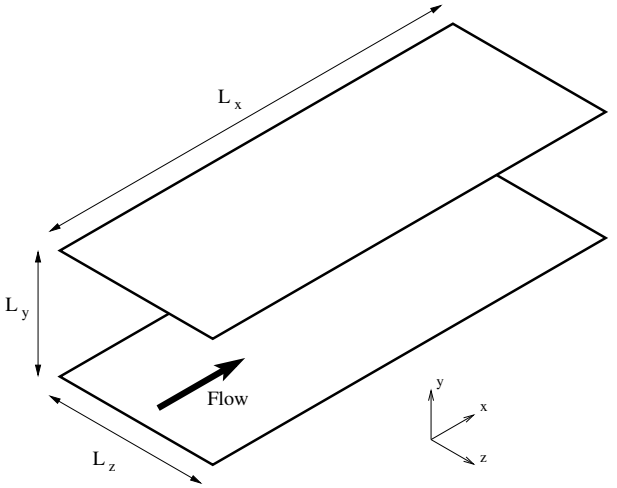

Fig. 10: Schematic of the computational domain of the channel flow.

5.1.2. Flow Conditions

The bulk velocity of the flow ($\overline{U}$), the channel half-height (δ), the bulk density ($\overline{\rho}$), and the wall temperature (T_w) are taken as the reference velocity, reference length, reference density, and reference temperature, respectively. The friction Reynolds number is defined by $Re_\tau = u_\tau \delta/\nu$, where ν is the fluid's kinematic viscosity and

$$u_\tau = \sqrt{\frac{\nu \left.\frac{\partial u}{\partial y}\right|_{\text{wall}}}{Re_f}} \tag{29}$$

is the friction velocity. All present channel flow simulations are performed at $Re_\tau \approx 544$. The exact value of the friction Reynolds number varies for each case based on the calculated slope of the streamwise velocity adjacent to the wall. This friction Reynolds number corresponds to a reference Reynolds number of $Re_f = 10{,}000$ based on the reference scales. The reference Mach number, based on the reference temperature and velocity, is $M_f = 0.4$. The heat capacity ratio is assumed fixed at $\gamma = 1.4$ for air, and the reference Prandtl number is $Pr = 0.72$.

The flow in a physical channel is normally driven by a negative pressure gradient in the streamwise direction ($\mathrm{d}p/\mathrm{d}x$). Here, a force term, which is dynamically adjusted, is applied to retain a constant mass flow rate. The forcing algorithm employed in the present work was introduced by Lenormand *et al.* [47].

Case	P	Number of elements	Number of grid points	Total grid points	y^+_{min}	Points in y^+_{10}	λ	$\Delta t \times 10^4$
P6-B	6	$20 \times 12 \times 30$	$140 \times 84 \times 210$	2,469,600	0.167	5	4.5	6.81
P6-H	6	$28 \times 17 \times 42$	$196 \times 119 \times 294$	6,857,256	0.121	8	4.3	5.07
P10-B	10	$13 \times 7 \times 19$	$143 \times 77 \times 209$	2,301,299	0.157	4	4.5	5.96
P10-H	10	$20 \times 12 \times 30$	$220 \times 132 \times 330$	9,583,200	0.068	7	4.5	2.84

Table 1: Details of the grids used for different cases of LES of the channel flow. Points in y^+_{10} is the number of grid points below $y^+ = 10$ near the wall, and Δt is the average time step size required for each grid.

5.1.3. Grid Resolution

The grid used for the LES of the periodic channel flow (shown in Fig. 11) has 20, 12, and 30 elements in the streamwise, wall-normal, and spanwise directions, respectively. The polynomial order of the basis functions within the elements is $P = 6$. This results in a total of 2,469,600 Gauss collocation points. The elements are uniformly distributed in the periodic directions (x and z). A hyperbolic tangent function of the form

$$\frac{y_n}{L_y} = \frac{1}{2}\left(1 - \frac{\tanh\left[\lambda(\frac{1}{2} - \frac{n}{N_y})\right]}{\tanh\left[\lambda/2\right]}\right), \quad n = 0, \ldots, N_y\,, \tag{30}$$

is used for the distribution of the elements in wall-normal direction. In Eq. (30), y_n is the location of the interfaces of the elements in the y-direction, N_y is the number of elements in the y-direction, and λ is an adjustable coefficient that determines the compactness of the elements adjacent to the walls. The average grid (Gauss points) spacings in the periodic directions in wall units are $\overline{\Delta x^+} \approx 49$ and $\overline{\Delta z^+} \approx 16$, and the wall-normal grid spacing ranges in $0.17 < \Delta y^+ < 43$. The details of the grid is included in Table 1; the grid used in this section is labeled as *P6-B*.

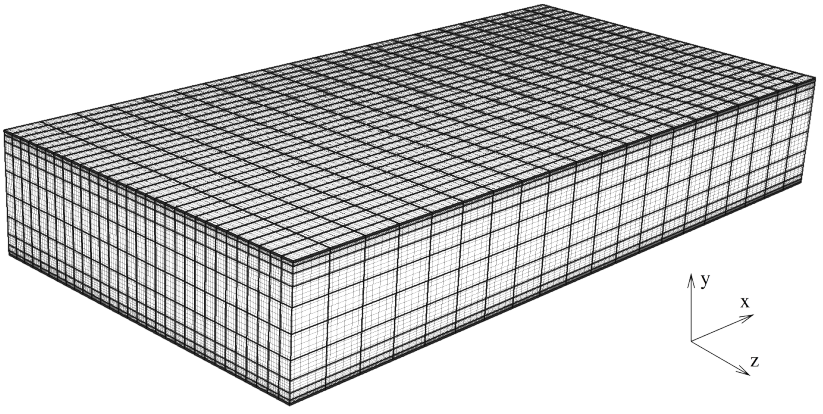

Fig. 11: The grid used for LES of the channel flow (grid P6-B). The element interfaces are shown with black lines, while the intersections of the gray lines indicate the locations of the Gauss grid points.

5.1.4. Initialization and Transition to Turbulence

The streamwise velocity is initialized with a laminar parabolic profile with a mean value of $\overline{U_0}$ as

$$u_0(y) = -6\left[\left(\frac{y}{2}\right)^2 - \left(\frac{y}{2}\right)\right](1 + \epsilon), \tag{31}$$

where ϵ is a 10% random disturbance intended to help accelerate the transition to turbulence. The spanwise and wall-normal velocities are initialized as zero. The initial temperature follows a laminar Poiseuille profile as

$$T(y) = T_w + \frac{3(\gamma - 1)}{4} Pr_f M_f [1 - (y - 1)^4]. \tag{32}$$

The density is initialized at $\rho_0 = 1$, and the initial pressure is calculated from the equation of state.

Our preliminary tests showed that the initial disturbance that is introduced to expedite the transition to turbulence gradually decays, and the transition does not occur. Neither an increase in the magnitude of the initial disturbance nor a temporary increase in the Reynolds number resulted in a transition to turbulence. Instead, the simulation is started using a significantly coarse grid with a polynomial order of $P = 2$ compared to the original order of $P = 6$. The truncation error caused by the low resolution is sufficiently large to provide the necessary disturbance for the transition to turbulence. Once the transition completes, the solution is spectrally interpolated to a new grid with higher resolution ($P = 3$), and the simulation is continued at the new resolution for a few flow-through times. To ensure stability, the solution is interpolated gradually to higher resolution grids using the same approach until reaching the desired resolution of $P = 6$. More details of the transition procedure and initialization are provided in Jacobs [28] and Ghiasi *et al.* [48].

5.2. Results

LES of the periodic channel flow has been performed using the modal filtering procedure. Different tests have been conducted, and the results are compared with the DNS of Lee and Moser [44], which is used as the reference in this study.

The rms velocity fluctuation in the x_i-direction is defined as $u''_{i,rms} = \{u''_i u''_i\}^{1/2}$, and the scaled rms velocity fluctuation is $u''^{+}_{i,rms} = u''_{i,rms}/u_\tau$. Here, $\{\}$ is the Favre average, which is defined by $\{f\} = \langle \rho f \rangle / \langle \rho \rangle$, where $\langle\rangle$ is the Reynolds (ensemble) average. Also, the single prime, $'$, and double prime, $''$, denote the turbulent fluctuations with respect to the Reynolds and Favre averages, respectively.

A case using the dynamic Smagorinsky model [8] is also simulated for comparison. The value of the dynamic Smagorinsky coefficient, C_s, is averaged within each element in the periodic directions to ensure stability [19].

Before performing the LES of the channel flow using the modal filter, we examined the amplitudes of the modes for the coarse DNS (no-model) case. The amplitude of the nth mode in element m, is denoted by $A_m(n)$ and is defined by Eq. (28) (See Fig. 5). We expect this quantity to be statistically only a function of the distance of the element from the wall. Hence, we categorize the elements into three levels: Level 1: elements adjacent to the wall, level 2: elements that are one element away from the wall, until level 6: elements nearest to the core of the channel. Then, we average the amplitudes of each mode over all elements within the same level to obtain $A_{\text{Level\_}l}(n)$, where $l = 1, \ldots, 6$.

Figure 12 presents the amplitudes of the modes of the streamwise velocity at different levels. The zeroth mode represents the bulk value of the quantity (streamwise velocity). The amplitude of this mode is greater for the higher levels (see $n = 0$) because the magnitude of the streamwise velocity is higher away from the wall. In contrast, the higher modes ($n > 0$) represent the spatial change of the quantity (streamwise velocity). The amplitudes of these modes are lower for the higher levels because the spatial changes of the streamwise velocity decrease as we get closer to the core of the channel. It is also observed that regardless of the distance from the wall, the amplitudes of the modes decrease exponentially for successive modes.

5.2.1. Filtering Strategy

As mentioned before, the filters were applied at every time step to the density, all three components of velocity, and pressure in the simulations of the isotropic turbulence. Our preliminary tests with the channel flow revealed that applying the filter at every time step results in excessively dissipated turbulence and incorrect statistics (not shown). Further tests showed that applying the filter every 100 time steps (equivalent to approximately 0.07 time units) provides good agreement with DNS (shown in the next section).

Then, we studied the effect of applying a weaker filter, by blending the filtered values with the unfiltered values, more frequently. Here, we apply the isotropic modal filter with $N_f = 1$ at different frequencies: $f = 1$, 0.1, 0.02, and 0.01 (the unit of the frequency is 1/time step), which correspond to filtering every 1, 10, 50, and 100 time steps, respectively. In order to maintain the overall strength of the filter in all these cases, a function is used to update the solution values with a combination of the filtered values and the original values [17]. The solution values are updated to the effective value of

$$Q_{\text{eff}} = \alpha\, Q_{\text{filt}} + (1 - \alpha)\, Q_{\text{orig}}, \tag{33}$$

where Q_{filt} and Q_{orig} are the filtered and original values, respectively. By choosing the combination coefficient to be $\alpha = 1$, we can disable the effect of the combination function, which was the case for previous simulations. Here, the value of α is chosen to be 0.01, 0.1, 0.5, and 1 for the cases with $f = 1$, 0.1, 0.02, and 0.01, respectively. Therefore, the cumulative strength of the filter, which is defined by $f \times \alpha$, remains the same for all cases.

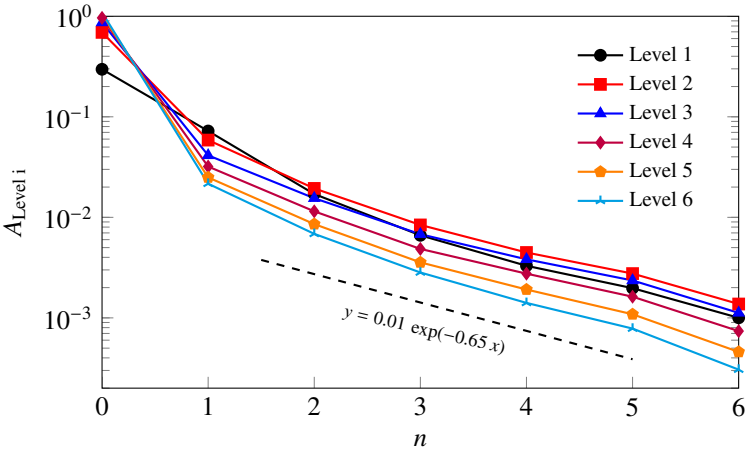

Fig. 12: The magnitude of the modes of the streamwise velocity in the coarse DNS of the channel flow. Lower level number indicates elements closer to the walls.

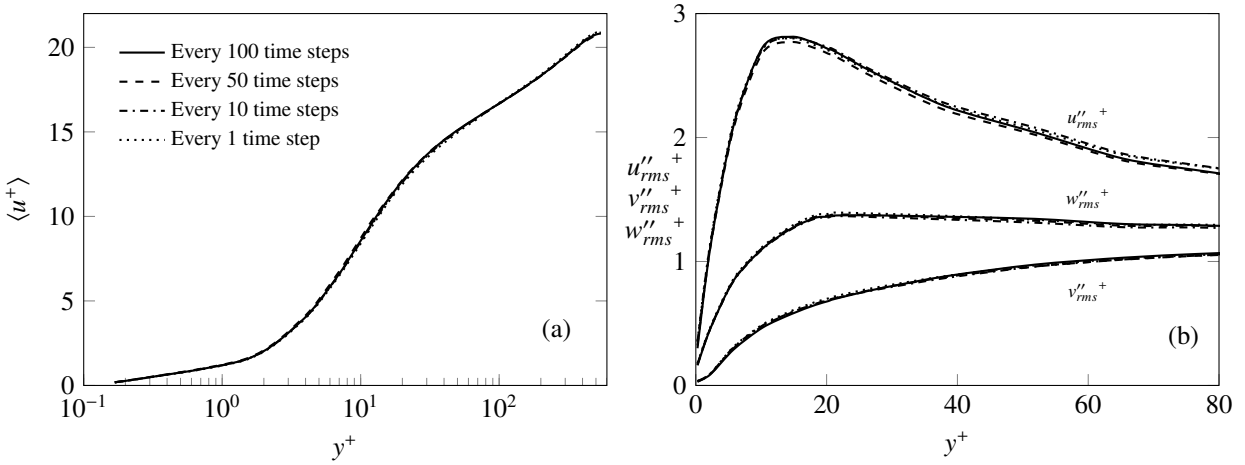

Fig. 13: (a) Mean streamwise velocity and (b) rms velocity fluctuations of LES of the channel flow using modal filter with $N_f = 1$ applied at different frequencies.

Figure 13 depicts the scaled mean streamwise velocity and rms velocity fluctuations for the four different frequencies of the modal filter. It is observed that the frequency of the filter has nearly no effect on the first- and second-order statistics of the flow, while the cumulative strength of the filter is maintained. Therefore, for all present simulations of the channel flow using the modal filter, the filter is applied to density, all three components of velocity, and pressure every 100 time steps, without blending ($\alpha = 1$).

5.2.2. Isotropic Modal Filter

The isotropic modal filtering is applied for $N_f = 1$ and 2, which correspond to removing one and two modes with highest frequencies, respectively. Since this filter, according to Eq. (16), removes the high-frequency modes in all three directions, it is called an isotropic modal filter. Figure 14 shows the scaled mean streamwise velocity, $\langle u^+ \rangle$, as a function of the distance from the wall in wall units, y^+. The profiles are compared with those from DNS, Coarse DNS, and the dynamic model. The difference between the DNS results and other cases in $0.1 < y^+ < 4$ are related to the plotting method; other cases have fewer solution points near the wall than DNS, and the solution values are connected by straight lines. It is observed that all cases predict the same velocity profile up to $y^+ \approx 8$. Further away from the wall, the case with no model (coarse DNS) underpredicts the mean velocity profile, the modal filtering with $N_f = 2$ overpredicts the profile, the dynamic model predicts close values to DNS, and the modal filtering with $N_f = 1$ provides excellent agreement with DNS. In fact, it shows slightly better velocity prediction than the dynamic model.

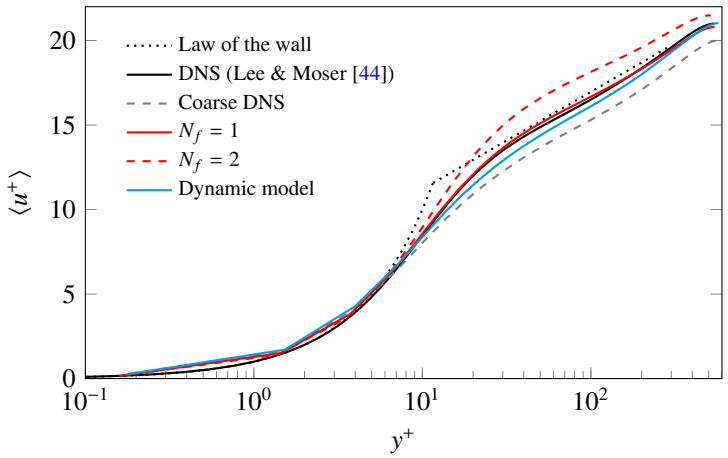

Fig. 14: Mean streamwise velocity for the LES of the channel flow using the modal filtering with different strengths. The DNS of Lee and Moser [44] is used as the reference.

The friction Reynolds numbers for all cases are provided in Table 2. The simulations in this section appear under the *base resolution* in the table. The closest prediction of the friction Reynolds number relative to the DNS value is provided by the modal filter with $N_f = 1$ with only 1.43% error. The modal filter with $N_f = 2$ and the case with no model significantly underpredict and overpredict the quantity, respectively. A large error in calculation of the friction Reynolds number indicates the inability to accurately calculate the slope of the mean velocity at the wall.

The rms of velocity fluctuations are shown in Fig. 15. The modal filter with $N_f = 1$, as well as the dynamic model, give good predictions of the streamwise component (Fig. 15(a)) as compared with DNS. With $N_f = 2$, however, the streamwise rms is significantly overpredicted for $y^+ > 7$. The coarse DNS also overpredicts the quantity near the wall ($y^+ < 10$). A closer look at the near-wall region reveals that the modal filtering provides better streamwise rms than the dynamic model, regardless of the filter strength (N_f). The reason the profiles do not meet at the axis origin ($\{0, 0\}$) is that the solutions are calculated on the Gauss grid points, and these collocation points, according to Eq. (9), do not exist on the element boundaries. The modal filtering with $N_f = 1$ as well as the dynamic model predict close values of wall-normal rms as shown in Fig. 15(b). The modal filter with $N_f = 2$ and the coarse DNS case underpredict and overpredict the profile, respectively. All present turbulence models do improve the prediction of the rms of velocity in the spanwise direction (Fig. 15(c)), compared to the coarse DNS case. It is observed that modal filtering, with $N_f = 2$, has excellent agreement with DNS near the wall ($y^+ < 30$), while $N_f = 1$ gives better prediction at regions away from the wall ($y^+ > 40$). This implies that stronger modal filtering is desired more near the wall than it is away from the wall.

5.2.3. Grid Independence Study

The simulation of the periodic channel flow with the base resolution (grid P6-B) that is presented in section 5.2.2 is performed using a grid with higher resolution to ensure the grid independency. The case that provide the closest results to DNS, i.e. $N_f = 1$, is chosen for the grid resolution study. A new grid with higher number of elements in all three directions that features the same polynomial order of $P = 6$ is considered. The high-resolution grid has 28, 17, and 42 elements in the streamwise, wall-normal, and spanwise directions, respectively. The details of this grid is included in Table 1 under case *P6-H*.

Figure 16 compares the mean streamwise velocity and rms velocity fluctuations based on the base and high resolution grids. It is observed that the mean and fluctuations of the velocity do not significantly change by increasing the resolution.

5.2.4. Filter Strength (N_f)

In the simulations presented in the previous sections, it was observed that the best agreement with DNS is obtained by the choice of $N_f = 1$. One may ask the questions: Is $N_f = 1$ always the best choice? What factors determine the correct choice of the filter strength (N_f)? To answer these questions, we perform some tests and study the effect of the polynomial order and h-resolution on the best choice of N_f. We consider two polynomial orders of $P = 6$ and 10,

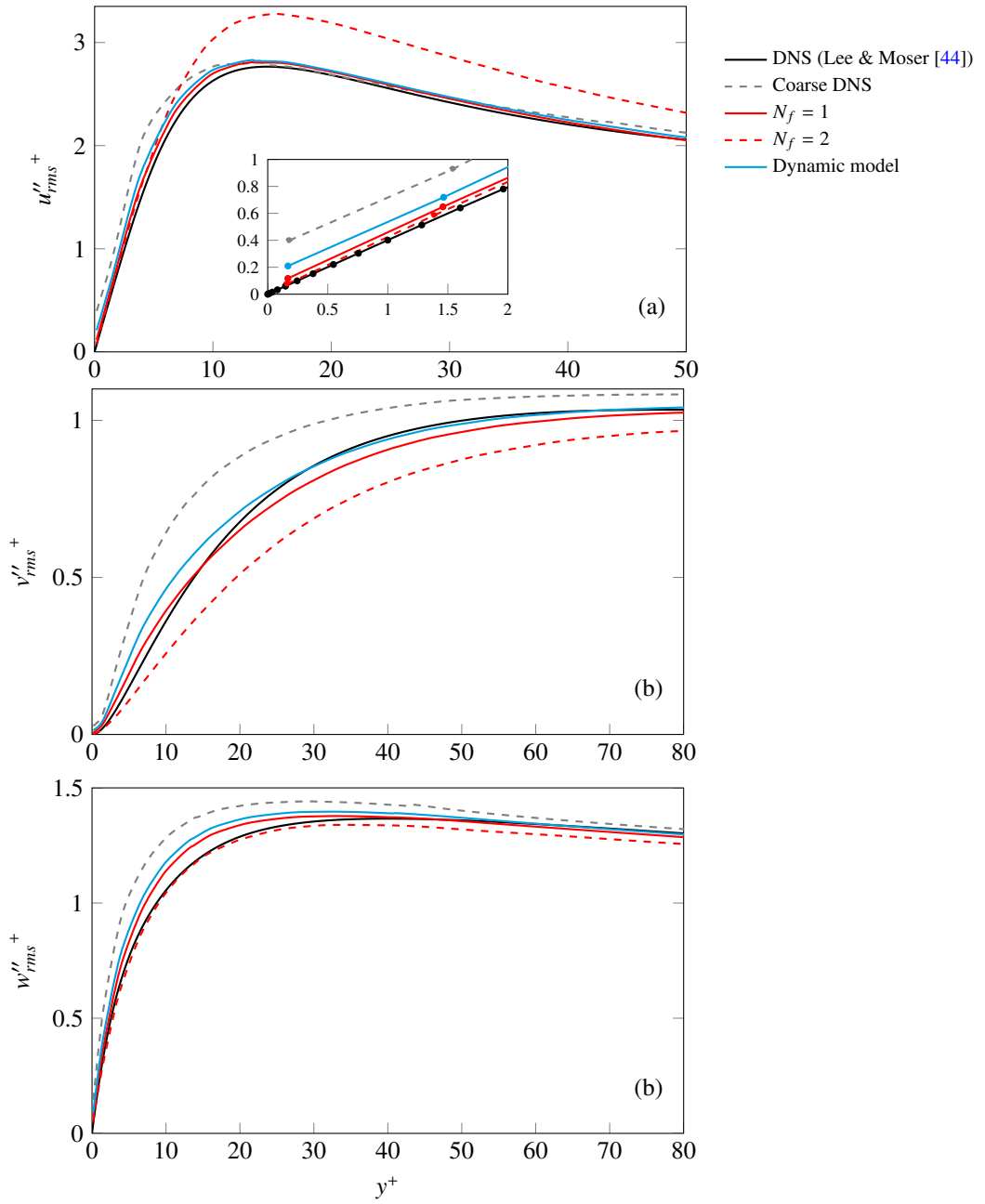

Fig. 15: Rms velocity fluctuations for the channel flow in the (a) streamwise (with magnified near-wall region), (b) wall-normal, and (c) spanwise directions using the modal filtering. The profiles are compared with DNS of Lee and Moser [44], coarse DNS, and the dynamic model.

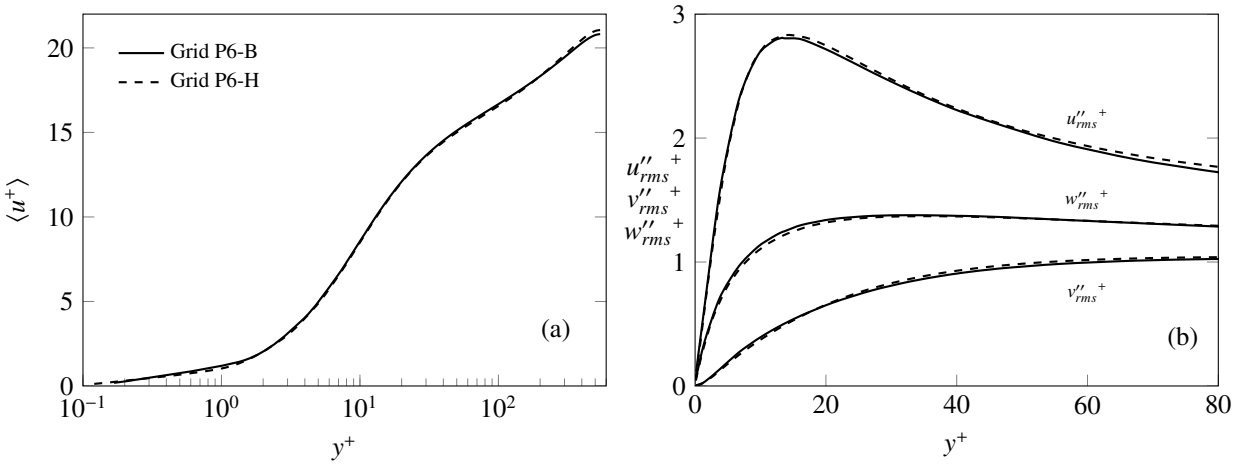

Fig. 16: Comparison of (a) mean streamwise velocity and (b) rms velocity fluctuations of LES of the channel flow with modal filter with $N_f = 1$ using the base (grid P6-B) and high resolution (grid P6-H) grids.

	Base resolution		High resolution	
N_f	Re_τ	Error	Re_τ	Error
0	575.5	5.79 %	558.6	2.68 %
1	545.4	0.26 %	543.2	-0.15 %
2	517.1	−4.95 %	527.9	−2.96 %

Table 2: The friction Reynolds numbers predicted by $P6$ cases as compared with DNS value of $Re_\tau = 544$. Note that $N_f = 0$ means a coarse DNS with no modal filter.

and for each P, we consider two grids with different h-resolutions. The details of the four grids are included in Table 1. For each of the four grids, we perform the LES using different modal filter strengths (N_f) and compare the results.

Table 2 presents the friction Reynolds numbers for all cases with $P = 6$. It is observed that for both resolutions, the friction Reynolds number decreases by increasing the filter strength. The important observation here is that regardless of the h-resolution, the smallest error with respect to the DNS case is obtained by $N_f = 1$. Table 3 presents the same quantity for cases with $P = 10$. The decrease in the friction Reynolds number by increasing the filter strength is again observed for $P = 10$. It is also shown that the best agreement with DNS is achieved using $N_f = 3$, again regardless of the h-resolution.

Figure 17(a) compares the mean velocity profiles of the channel flow for the cases of the modal filter with different strengths (N_f) that are performed on the base resolution grid with $P = 6$ (grid P6-B). It is observed that the best comparison with DNS is obtained by $N_f = 1$. Figure 17(b) presents the same velocity profile for the high resolution

	Base resolution		High resolution	
N_f	Re_τ	Error	Re_τ	Error
0	587.0	7.90 %	559.2	2.79 %
1	563.0	3.50 %	553.0	1.65 %
2	551.7	1.41 %	549.7	1.05 %
3	543.0	-0.18 %	544.7	0.13 %
4			539.2	−0.89 %
5			533.6	−1.92%

Table 3: The friction Reynolds numbers predicted by $P10$ cases as compared with DNS value of $Re_\tau = 544$. Note that $N_f = 0$ means a coarse DNS with no modal filter.

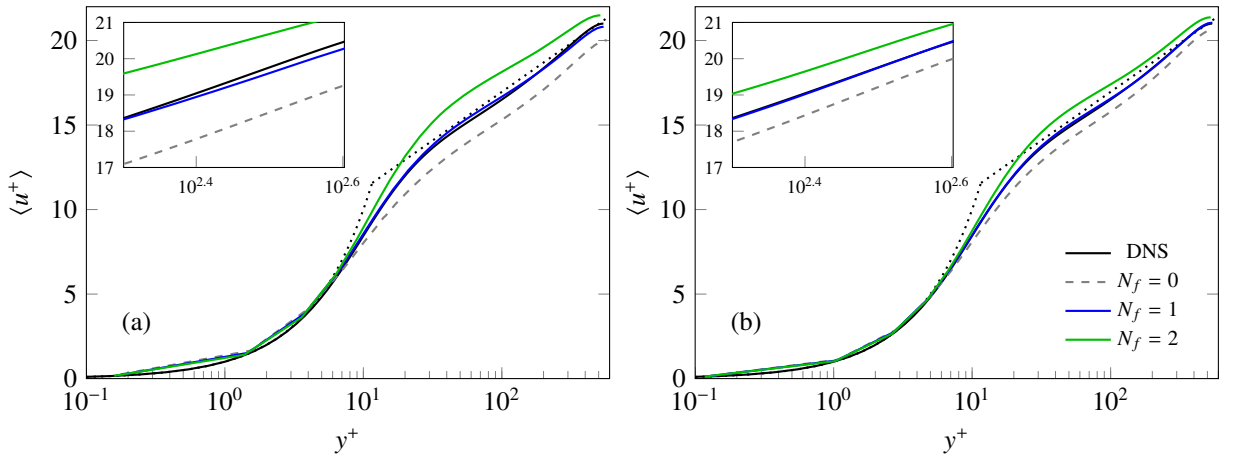

Fig. 17: Mean streamwise velocity for the LES of the channel flow with $P = 6$ using the modal filter with different strengths (N_f) based on (a) the base resolution grid (P6-B) and (b) the high resolution grid (P6-H). The DNS of Lee and Moser [44] is used as the reference. The boxes inside the plots show magnified versions.

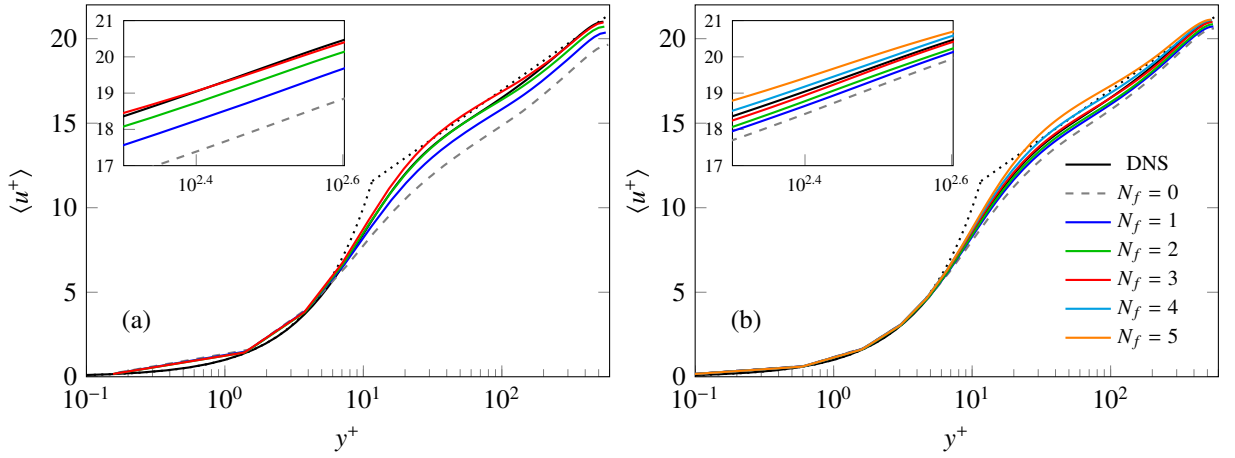

Fig. 18: Mean streamwise velocity for the LES of the channel flow with $P = 10$ using the modal filter with different strengths (N_f) based on (a) the base resolution grid (P10-B) and (b) the high resolution grid (P10-H). The DNS of Lee and Moser [44] is used as the reference. The boxes inside the plots show magnified versions.

grid (P6-H). The closest profile to that of the DNS case is again obtained by $N_f = 1$. The results for $P = 10$ are presented in Fig. 17(a) and (b). It is observed that, for both resolutions, the best agreement with DNS is provided by $N_f = 3$. The important observation here is that the same value of N_f is the best choice for both h-resolutions as long as the polynomial order is the same. Therefore, the choice of N_f is dependent on only the polynomial order, and not on the h-resolution. However, regardless of P and N_f, increasing the h-resoltion improves the predictions of friction Reynolds number and mean velocity.

5.2.5. Anisotropic Modal Filter

In the previous sections, the modal filter formulated by Eq. (16) was applied to the solution variables in the channel flow. This filter is the same as that applied to the isotropic turbulence case in section 4 and removes high-frequency modes from all three directions equally. Since the channel flow is not an isotropic flow, we applied an anisotropic version of the modal filter to determine the sensitivity of the results to the direction of the filter. The anisotropic modal filter, given by Eq. (17), removes the motions with contributions from the highest-frequency modes in only one direction. In this section, the anisotropic modal filter, with $N_f = 1$, is applied in three different directions for LES of the channel flow (using grid P6-B), and the results are compared with the isotropic filter as well as DNS and coarse DNS cases. The choice of $N_f = 1$ is due to its superior performance with the isotropic modal filter for the channel

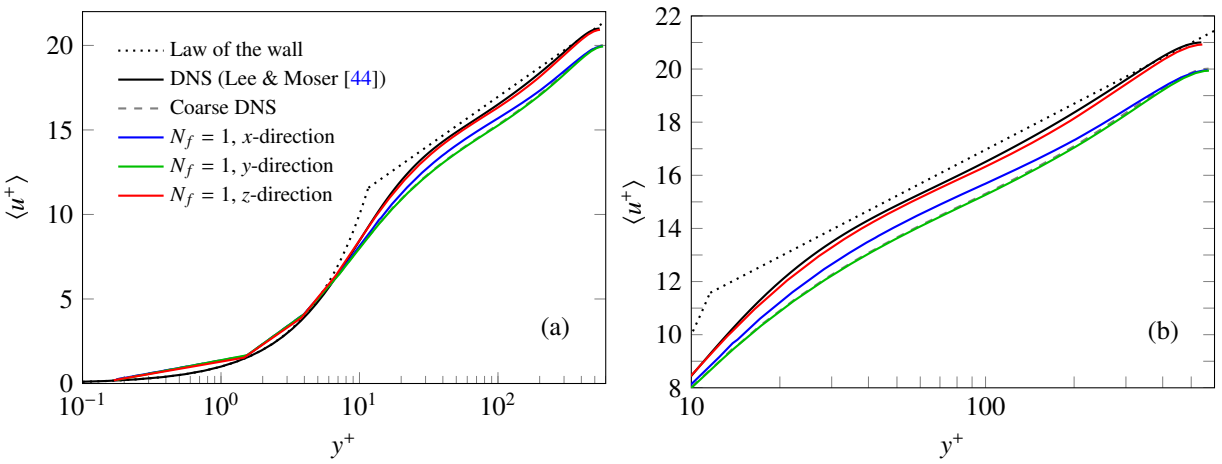

Fig. 19: (a) Mean streamwise velocity for the LES of the channel flow using the modal filtering applied in different directions. (b) Same as (a), but magnified at the log-law region. The DNS of Lee and Moser [44] is used as the reference.

Case	Re_τ	Error
DNS	544	-
Anisotropic modal (x-direction)	571.0	4.95 %
Anisotropic modal (y-direction)	577.1	6.08 %
Anisotropic modal (z-direction)	547.9	0.72 %

Table 4: The friction Reynolds numbers for the non-isotropic modal filtering cases as compared with DNS.

flow.

Figure 19 shows the mean streamwise velocity profiles of the LES of channel flow using the anisotropic modal filtering with $N_f = 1$ applied in the three directions. It is observed that applying the modal filter in the spanwise (z) direction provides the closest profile to DNS. Applying the filter in the streamwise (x) direction has a slight effect on the profile, and applying it in the wall-normal (y) direction has nearly no effect on the profile, i.e., the mean velocity is the same as the coarse DNS case.

The values of the friction Reynolds number for cases with the anisotropic modal filter are presented in Table 4. Again, the prediction of the friction Reynolds number closest to the DNS result is provided by the anisotropic filter applied in the spanwise direction.

The rms velocity fluctuations are shown in Fig. 20. It is observed that applying the filter in the y-direction has nearly no effects on the velocity fluctuations in any direction. Applying the filter in the x-direction slightly improves the predictions of the spanwise and wall-normal fluctuations. However, applying the filter in the z-direction, i.e., removing one mode in the spanwise direction, noticeably improves the rms profiles in all three directions.

We also observed previously that the modal filtering in LES of the channel flow is most effective in accurate prediction of the mean velocity and the friction Reynolds number when one mode is removed from the spanwise direction. These observations are consistent with the fact that the motions in the spanwise direction contain more energy than the motions in the streamwise direction as demonstrated in Fig. 21(a)-(c). This figure shows the one-dimensional energy spectra along two periodic directions based on the three components of the velocity. The 1D enegy spectra are defined as

$$E(k) = \frac{1}{\pi} \int_{-\infty}^{\infty} R(x)\, e^{-ikx}\ \mathrm{d}x, \tag{34}$$

where $R(x)$ is the two-point correlation defined by

$$R(x) = \langle u(x_0, t)\, u(x_0 + x, t) \rangle. \tag{35}$$

The spectra in Fig. 21 are measured at three different distances from the wall: near-wall region ($y^+ \approx 6$), midrange ($y^+ \approx 15$), and the core of the channel ($y^+ \approx 170$). It is observed that the spectra in the spanwise direction (solid

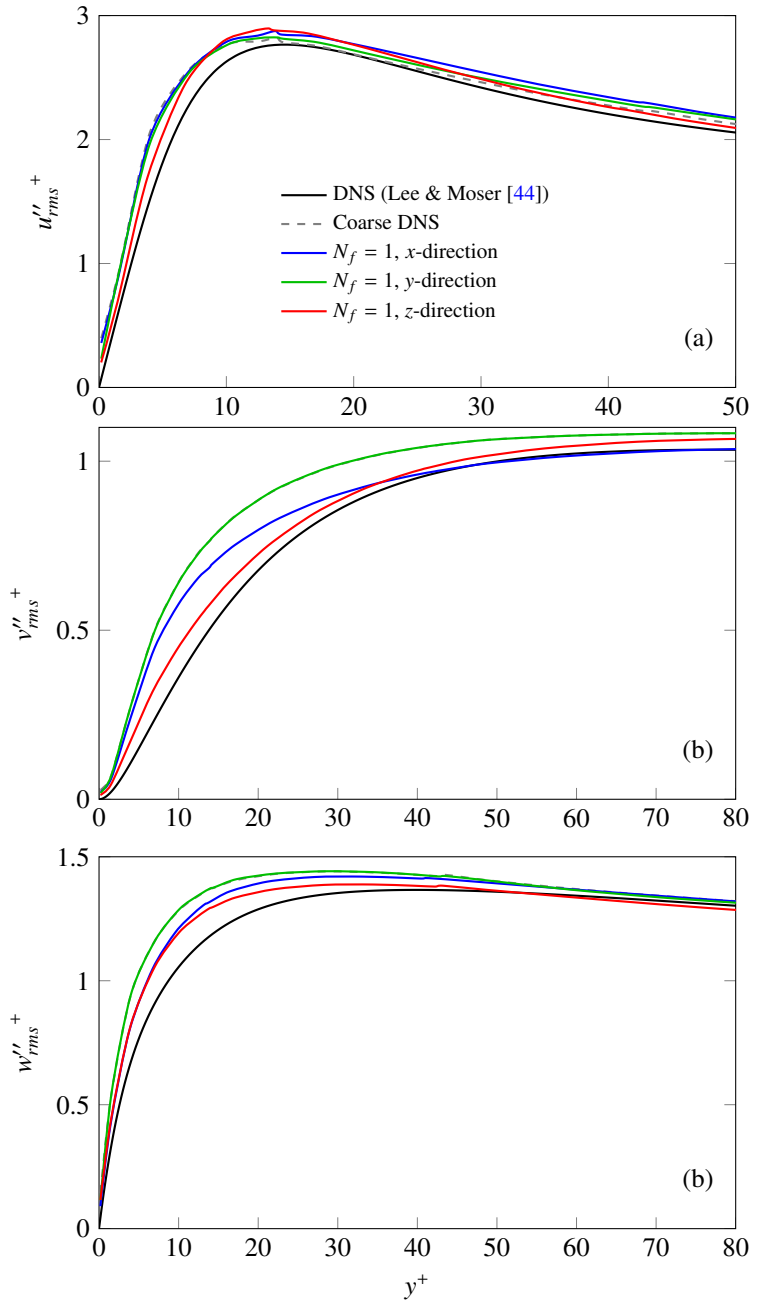

Fig. 20: Rms fluctuations of the (a) streamwise, (b) wall-normal, and (c) spanwise velocity components for the LES of channel flow using the modal filtering applied in different directions, as compared with DNS and coarse DNS.

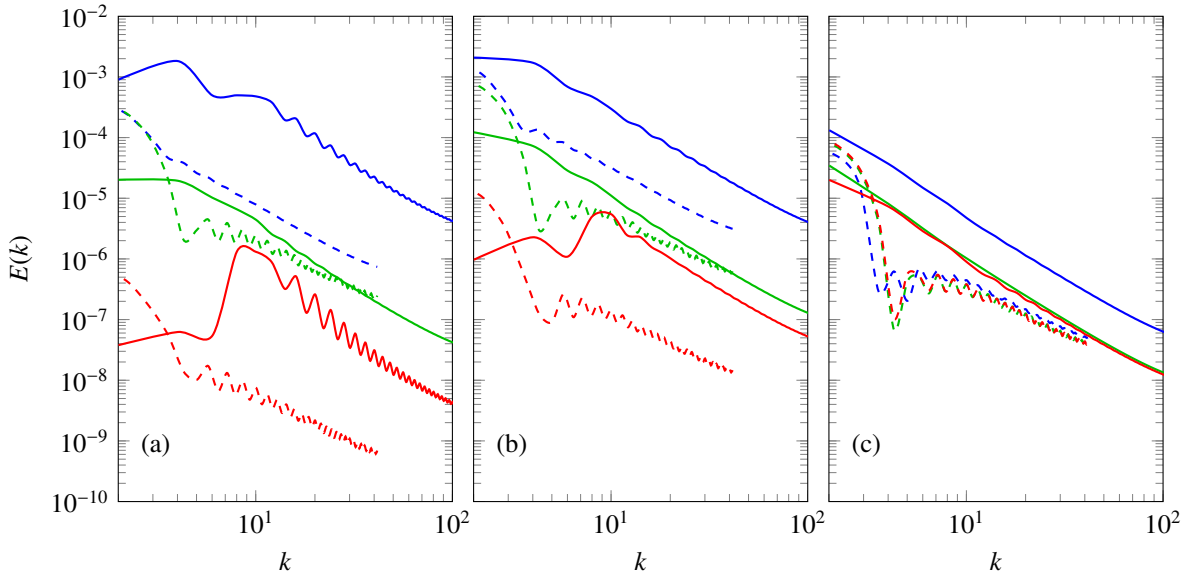

Fig. 21: One-dimensional energy spectra for the coarse DNS of the channel flow based on the streamwise (blue), wall-normal (green), and spanwise (red) components of the velocity, along the periodic directions: streamwise (dashed) and spanwise (solid), at three distances from the wall: (a) $y^+ \approx 6$, (b) $y^+ \approx 15$, and (c) $y^+ \approx 170$.

curves) are higher than those in the streamwise direction (dashed curves), regardless of the distance from the wall or the component of the velocity. Therefore, there is a greater amount of energy in the spanwise direction that cascades to the higher-frequency motions and needs to be dissipated by the turbulence model at the cutoff wavenumber. This could contribute to the fact that removing the highest-frequency mode in the spanwise direction is more effective than it is in the streamwise direction. Note that the conclusion that filtering in the spanwise direction is the most effective among three directions is drawn merely for the periodic channel flow. Further investigation is needed to generalize this behavior for various near-wall flows.

We also examined and compared the amplitude of the highest-frequency modes in each direction. These quantities are defined by

$$\begin{cases} A_{q,x}(p) = \langle \hat{u}_{plm} \rangle \quad , \quad l = 0, \ldots, P \, , \quad m = 0, \ldots, P \\ A_{q,y}(p) = \langle \hat{u}_{kpm} \rangle \quad , \quad k = 0, \ldots, P \, , \quad m = 0, \ldots, P \, , \\ A_{q,z}(p) = \langle \hat{u}_{klp} \rangle \quad , \quad k = 0, \ldots, P \, , \quad l = 0, \ldots, P \end{cases} \tag{36}$$

for the highest-frequency modes in the x-, y-, and z-directions, respectively, in the element q. Again, we categorize the elements throughout the domain into six levels based on their distances from the wall. Then, we average the quantities defined in Eq. (36) over the elements within the same level to obtain $\langle A_x(p) \rangle$, $\langle A_y(p) \rangle$, and $\langle A_z(p) \rangle$ at each level. The amplitude of the highest-frequency mode in each direction is shown in Fig. 22 for three sample levels: 1, 3, and 5. It is observed that the amplitude of the highest-frequency modes is higher in the spanwise direction than it is in the other two directions. This is also identified as another reason why removing the highest-frequency modes in the spanwise direction is the most effective among three directions.

6. Computational Cost

The computational costs of the presented methods are quantified by running the same simulation using different models and measuring the run time. The LES of the isotropic turbulence is conducted for 10 time steps using the modal filter, series and 3D nodal filters, and the dynamic model. The run times are compared with a case without any turbulence model. Also, three polynomial orders of $P = 4$, 8, and 16 are considered to investigate the effect of P on the computational costs. The run times are averaged among 20 trials for each case. All simulations are performed using a single processor so that the results are not affected by the parallel efficiency of the code. Intel Xeon E5-2670 (2.60 GHz) processors are used.

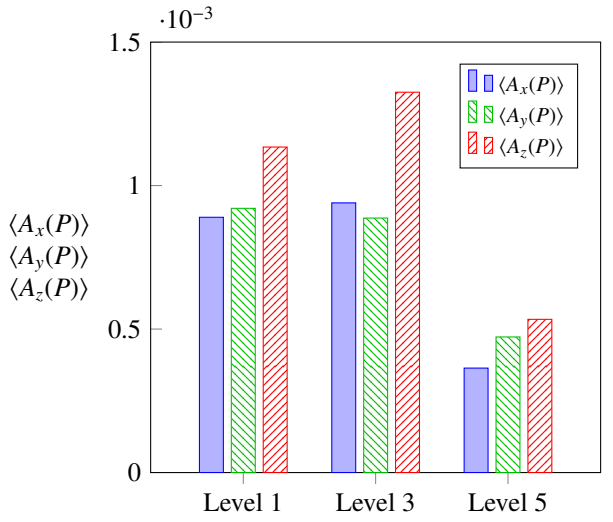

Fig. 22: Magnitude of the highest-frequency modes in each direction. Lower level means elements closer to the wall, and higher level indicates elements farther from the wall.

Case	P=4		P=8		P=12	
	Run time (s/time step)	Overhead (%)	Run time (s/time step)	Overhead (%)	Run time (s/time step)	Overhead (%)
No-model	0.875	-	4.85	-	14.73	-
Modal filter	0.898	2.55	4.94	1.93	14.80	0.45
Series nodal filter	0.910	3.93	5.04	4.01	15.35	4.18
3D nodal filter	0.900	2.85	5.01	3.40	15.49	5.12
Dynamic model	1.271	45.2	6.88	41.9	21.49	45.9

Table 5: Run times (seconds per time step) and computational overheads for the LES of the isotropic turbulence using different polynomial orders.

Table 5 presents the run times and the computational overheads for all cases as compared with the case with no model. The computational overheads are also depicted in Fig. 23. It is observed that the modal filter is the least computationally costly method among presented models regardless of the polynomial order. It is also the only model whose computational cost reduces for higher polynomial orders, with an overhead of only 0.45% for $P = 12$. This could be attributed to the computational implementation; *FFTW* library, which is known as one of the fastest fast Fourier transform (FFT) libraries [49], is used to implement the transformation of the solution between nodal and modal representations. The dynamic model is the most computationally expensive choice; all filtering procedures are at least one order of magnitude less costly than the dynamic model. Also, the computational cost of the dynamic model does not have a meaningful dependence on the polynomial order. The series nodal filter has a constant overhead of roughly 4%, while the cost of the 3D nodal filter increases for higher polynomial orders. The 3D nodal filter is less costly than the series version for the lower polynomial orders, and it is more costly for higher orders.

7. Summary and Conclusions

A modal low-pass filter is applied to a discontinuous spectral element method (DSEM), and its performance is compared with two types of interpolation-based nodal filters, series and 3D, and DNS for LES of turbulent flows with no additional SGS model. An isotropic decaying turbulence and a periodic turbulent channel flow are used as the test cases. The conclusions from the isotropic turbulence tests are as follows:

1. By removing the N_f highest-frequency modes using the modal filter, the solution becomes smoother step by step while increasing N_f, and the small-scale features are removed. However, by applying a nodal filter, especially

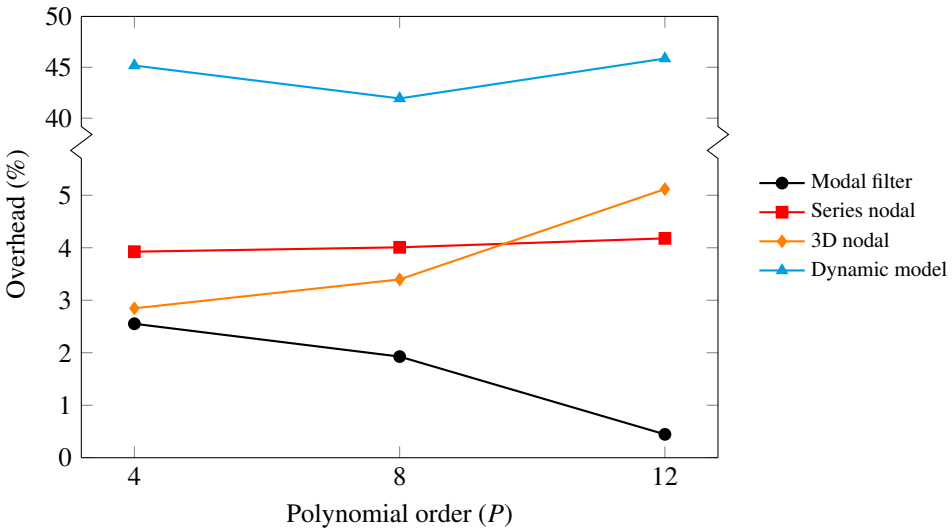

Fig. 23: Computational cost overheads of the presented models for the isotropic turbulence case at different polynomial orders.

for $N'_f > 2$, the shape of the function changes as well. The lower-frequency modes are also contaminated with nodal filters, except for the 3D nodal filter with $N'_f = 1$.

2. All filtering procedures provide better drop-off of the energy spectra at high wavenumbers compared with cases with no model. However, the nodal filters overpredict the spectra at the midrange and low wavenumbers. This overprediction is more severe in the series nodal filter than it is in the 3D version. Regardless of the filtering procedure, removing one mode provides the closest agreement with DNS.
3. The modal filter predicts the correct decay of the TKE for both $N_f = 1$ and 2. The series nodal filter underpredicts the rate of decay of turbulence regardless of N'_f. The 3D filter underpredicts the decay of TKE for $N'_f = 2$.

The modal filter provided more accurate statistics than the nodal filters in the isotropic turbulence tests. Therefore, this filtering procedure is chosen for further simulations. The modal filter, as well as an anisotropic version of the filter, is used in LES of a periodic turbulence channel flow. The conclusions are as follows:

1. The modal filtering procedure provides accurate statistics including the mean velocity, the friction Reynolds number, and velocity fluctuations, with respect to DNS.
2. The best choice of the filter strength (N_f) depends only on the polynomial order (P) and is independent of the h resolution. For a polynomial order of $P = 6$, a filter with $N_f = 1$ provides the best agreement with DNS, and for $P = 10$, the best results are obtained by $N_f = 3$, regardless of the grid resolution.
3. Applying a too strong filter results in an overprediction of the mean and fluctuations of the streamwise velocity and an underprediction of the friction Reynolds number and fluctuations of the wall-normal velocity. The opposite results are obtained by applying a too weak filter.
4. Removing the highest-frequency modes in the spanwise direction is the most effective among three directions and provides the closest predictions of the velocity profile and the rms velocity fluctuations to DNS results. This observation is attributed to (i) the fact that the one-dimensional energy spectra are higher in the spanwise direction than the streamwise direction, and (ii) the fact that the amplitude of the highest-frequency mode is larger in the spanwise direction than the other two directions.
5. The frequency of the application of the filter does not affect the first- and second-order statistics as long as the cumulative strength of the filter is maintained; the cumulative strength of the filter is controlled by a function that updates the solution with a combination of the filtered and original values.
6. The amplitudes of the modes of the channel flow field decrease exponentially for successive modes from low-frequency to high-frequency regardless of the distance from the walls.

It is also observed that all filtering procedures are significantly less computationally expensive than the dynamic model, while the modal filter is the fastest model. The dynamic Smagorinsky model introduces a computational

overhead of about 45%, while the other methods have less than 5% overhead. In general, the modal filter has shown good performance for both isotropic and wall-bounded flows; the calculated channel friction Reynolds number for the modal filter is within 0.26% error with respect to the DNS data, compared to 5.8% error for a case with no modeling.

Acknowledgement

The authors acknowledge the Advanced Cyberinfrastructure for Education and Research (ACER) group [50] at The University of Illinois at Chicago for providing high performance computing (HPC) resources that have contributed to the results reported in this paper. We would like to also thank the administration of XSEDE's supercomputer, Comet, who provided us with computational resources and technical support.

References

[1] O. V. Vasilyev, T. S. Lund, P. Moin, A general class of commutative filters for LES in complex geometries, J. Comput. Phys. 146 (1998) 82–104.
[2] J. Gullbrand, F. K. Chow, The effect of numerical errors and turbulence models in large-eddy simulations of channel flow, with and without explicit filtering, J. Fluid Mech. 495 (2003) 323–341.
[3] T. Lund, H. Kaltenbach, Experiments with explicit filtering for LES using a finite-difference method, Annual Research Briefs, Center for Turbulence Research, Stanford University (1995) 91–105.
[4] T. Lund, On the use of discrete filters for large eddy simulation, Annual Research Briefs, Center for Turbulence Research, Stanford University (1997) 83–95.
[5] G. S. Winckelmans, A. A. Wray, O. V. Vasilyev, H. Jeanmart, Explicit-filtering large-eddy simulation using the tensor-diffusivity model supplemented by a dynamic Smagorinsky term, Phys. Fluids 13 (2001) 1385–1403.
[6] D. K. Lilly, A proposed modification of the Germano subgrid-scale closure method, Phys. Fluids A: Fluid Dynamics 4 (1992) 633–635.
[7] J. Smagorinsky, General circulation experiments with the primitive equations. I. The basic experiment, Mon. Weather. Rev. 91 (1963) 99–164.
[8] M. Germano, U. Piomelli, P. Moin, W. H. Cabot, A dynamic subgrid-scale eddy viscosity model, Phys. Fluids A: Fluid Dynamics 3 (1991) 1760–1765.
[9] J. Bardina, J. H. Ferziger, W. C. Reynolds, Improved subgrid-scale models for large-eddy simulation, in: American Institute of Aeronautics and Astronautics, Fluid and Plasma Dynamics Conference, 13th, 1980, p. 10.
[10] F. F. Grinstein, C. Fureby, Recent progress on MILES for high Reynolds number flows, J. Fluids Eng. 124 (2002) 848–861.
[11] L. G. Margolin, W. J. Rider, F. F. Grinstein, Modeling turbulent flow with implicit LES, J. Turbul. (2006) N15.
[12] F. F. Grinstein, L. G. Margolin, W. J. Rider, Implicit large eddy simulation: computing turbulent fluid dynamics, Cambridge university press, 2007.
[13] A. Aspden, N. Nikiforakis, S. Dalziel, J. Bell, Analysis of implicit LES methods, Commu. Appl. Math. Comput. Sci. 3 (2009) 103–126.
[14] A. R. Winters, R. C. Moura, G. Mengaldo, G. J. Gassner, S. Walch, J. Peiro, S. J. Sherwin, A comparative study on polynomial dealiasing and split form discontinuous galerkin schemes for under-resolved turbulence computations, Journal of Computational Physics 372 (2018) 1–21.
[15] C. Bogey, C. Bailly, Computation of a high Reynolds number jet and its radiated noise using large eddy simulation based on explicit filtering, Comput. & Fluids 35 (2006) 1344–1358.
[16] J. Mathew, R. Lechner, H. Foysi, J. Sesterhenn, R. Friedrich, An explicit filtering method for large eddy simulation of compressible flows, Phys. Fluids 15 (2003) 2279–2289.
[17] P. Fischer, J. Mullen, Filter-based stabilization of spectral element methods, C. R. Acad. Sci. I-Math. 332 (2001) 265 – 270.
[18] P. Fischer, J. Lottes, A. Siegel, G. Palmiotti, Large eddy simulation of wire wrapped fuel pins i: hydrodynamics in a periodic array, in: Joint International Topical Meeting on Mathematics & Computation and Super computingin Nuclear Applications (M&C+ SNA 2007), 2007.
[19] K. Sengupta, Direct and large-eddy simulation of compressible flows with spectral/hp element methods, Ph.D. Thesis, University of Illinois at Chicago, 2008.
[20] H. Kanchi, F. Mashayek, K. Sengupta, G. Jacobs, P. Fischer, Comparison of LES studies in backward-facing step using Chebyshev multidomain and Legendre spectral element methods, in: AIAA Paper, 2011-3557, 2011.
[21] J. P. Boyd, The erfc-log filter and the asymptotics of the Euler and Vandeven sequence accelerations, in: Proceedings of the Third International Conference on Spectral and High Order Methods, Houst. J. Math., 1996, pp. 267–276.
[22] J. P. Boyd, Two comments on filtering (artificial viscosity) for Chebyshev and Legendre spectral and spectral element methods: preserving boundary conditions and interpretation of the filter as a diffusion, J. Comput. Phys. 143 (1998) 283–288.
[23] J. G. Levin, M. Iskandarani, D. B. Haidvogel, A spectral filtering procedure for eddy-resolving simulations with a spectral element ocean model, J. Comput. Phys. 137 (1997) 130–154.
[24] H. M. Blackburn, S. Schmidt, Spectral element filtering techniques for large-eddy simulation with dynamic estimation, J. Comput. Phys. 186 (2003) 610–629.
[25] R. Bouffanais, M. O. Deville, P. F. Fischer, E. Leriche, D. Weill, Large-eddy simulation of the lid-driven cubic cavity flow by the spectral element method, J. Sci. Comput. 27 (2006) 151–162.
[26] A. Chaudhuri, G. B. Jacobs, W.-S. Don, H. Abbassi, F. Mashayek, Explicit discontinuous spectral element method with entropy generation based artificial viscosity for shocked viscous flows, Journal of Computational Physics 332 (2017) 99–117.
[27] J. S. Mullen, P. F. Fischer, Filtering techniques for complex geometry fluid flows, Commun. Numer. Methods Eng. 15 (1999) 9–18.
[28] G. B. Jacobs, Numerical simulation of two-phase turbulent compressible flows with a multidomain spectral method, Ph.D. Thesis, University of Illinois at Chicago, 2003.

[29] D. A. Kopriva, J. H. Kolias, A conservative staggered-grid Chebyshev multidomain method for compressible flows, J. Comput. Phys. 125 (1996) 244–261.
[30] D. A. Kopriva, A staggered-grid multidomain spectral method for the compressible Navier–Stokes equations, J. Comput. Phys. 143 (1998) 125–158.
[31] D. Li, Z. Ghiasi, J. Komperda, F. Mashayek, The effect of inflow Mach number on the reattachment in subsonic flow over a backward-facing step, in: AIAA Paper, 2016-2077, 2016.
[32] Z. Ghiasi, J. Komperda, D. Li, F. Mashayek, Simulation of supersonic turbulent non-reactive flow in ramp-cavity combustor using a discontinuous spectral element method, in: AIAA Paper, 2016-0617, 2016.
[33] J. Komperda, Z. Ghiasi, D. Li, F. Mashayek, A. Irannejad, F. A. Jaberi, Simulation of the cold flow in a ramp-cavity combustor using a DSEM-LES/FMDF hybrid scheme, in: AIAA Paper, 2016-1938, 2016.
[34] Z. Ghiasi, D. Li, J. Komperda, F. Mashayek, Wall resolution study for direct numerical simulation of turbulent channel flow using a multidomain chebyshev grid, in: Tenth International Symposium on Turbulence and Shear Flow Phenomena, 2017.
[35] D. Li, Z. Ghiasi, J. Komperda, F. Mashayek, A numerical study of compressibility effects in turbulent mixing layer, in: Tenth International Symposium on Turbulence and Shear Flow Phenomena, 2017.
[36] J. Hesthaven, T. Warburton, Nodal discontinuous Galerkin methods: algorithms, analysis, and applications, Springer Science & Business Media, Berlin, 2008.
[37] P. Corr, D. Stewart, P. Hanna, J. Ming, F. J. Smith, Discrete Chebyshev transform. A natural modification of the DCT, in: Pattern Recognition, 2000. Proceedings. 15th International Conference on, volume 3, IEEE, 2000, pp. 1142–1145.
[38] FFTW documentations: 1d Real-even DFTs (DCTs), http://www.fftw.org/fftw3_doc/1d-Real_002deven-DFTs-_0028DCTs_0029.html, Accessed: 2017-09-07.
[39] P. F. Fischer, G. W. Kruse, F. Loth, Spectral element methods for transitional flows in complex geometries, J. Sci. Comput. 17 (2002) 81–98.
[40] G. A. Blaisdell, N. N. Mansour, W. C. Reynolds, Compressibility effects on the growth and structure of homogeneous turbulent shear flow, J. Fluid Mech. 256 (1993) 443–485.
[41] G. A. Blaisdell, N. N. Mansour, W. C. Reynolds, Numerical simulation of compressible homogeneous turbulence, Advances in Compressible Turbulent Mixing TF-50, Stanford University, Stanford, CA, 1992.
[42] G. B. Jacobs, D. A. Kopriva, F. Mashayek, Validation study of a multidomain spectral code for simulation of turbulent flows, AIAA J. 43 (2005) 1256–1264.
[43] J. Gullbrand, Explicit filtering and subgrid-scale models in turbulent channel flow, Annual Research Briefs, Center for Turbulence Research, Stanford University (2001) 31–42.
[44] M. Lee, R. D. Moser, Direct numerical simulation of turbulent channel flow up to $Re_\tau \approx 5200$, Journal of Fluid Mechanics 774 (2015) 395–415.
[45] M. M. Rai, P. Moin, Direct simulations of turbulent flow using finite-difference schemes, Journal of Computational Physics 96 (1991) 15–53.
[46] J. Kim, P. Moin, R. D. Moser, Turbulent statistics in fully developed turbulent channel flow at low Reynolds number, Journal of Fluid Mechanics 177 (1987) 133–166.
[47] E. Lenormand, P. Sagaut, L. Ta Phuoc, Large eddy simulation of subsonic and supersonic channel flow at moderate Reynolds number, Int. J. Numer. Methods Fluids 32 (2000) 369–406.
[48] Z. Ghiasi, D. Li, J. Komperda, F. Mashayek, Near-wall resolution requirement for direct numerical simulation of turbulent flow using multidomain Chebyshev grid, International Journal of Heat and Mass Transfer 126 (2018) 746 – 760.
[49] FFT benchmark results, http://http://www.fftw.org/speed/, Accessed: 2017-09-07.
[50] Advanced Cyberinfrastructure for Education and Research, http://acer.uic.edu/, Accessed: 2017-10-01.